

Carleton University

INVESTIGATION OF ALL-DIELECTRIC HUYGENS' METASURFACES AT
MILLIMETER-WAVE FREQUENCIES

KIMI MAHESHWARI
DEPARTMENT OF ELECTRONICS
Carleton University

thesis submitted to the Faculty of Graduate and Postdoctoral Affairs in partial fulfillment
of the requirements for the degree of
MASTER OF APPLIED SCIENCE
(ELECTRICAL AND COMPUTER ENGINEERING)
APRIL 2019

Carleton University

This thesis titled:

INVESTIGATION OF ALL-DIELECTRIC HUYGENS' METASURFACES AT
MILLIMETER-WAVE FREQUENCIES

presented by: MAHESHWARI Kimi
to obtain the degree of : Masters of Applied Science
Evaluated by the thesis committee consisting of:

M. PAVAN Gunupudi, Doct., President
M. GUPTA Shulabh, Ph. D., Research Supervisor
M. DEREK McNamara, Ph. D., External Member
M. TOM Smy, Ph. D., Internal Member

Acknowledgements

First and foremost, I would like to thank my supervisor Prof. Shulabh Gupta, for whom I owe a great deal of gratitude. Having been away from studies for six years, I was academically rusty when I started. In addition to his guidance, Prof. Gupta allowed me the time to ease back into this field and provided unconditional support. Without his patient guidance over these two years, I would have stranded many times over.

I would like to thank members of my research group, Daniel King, Joseph Botros, Mohamed Emara, Muhammad Ali and Vijay Sharma, for offering their help and support and providing me feedback during our group meetings. I would also like to acknowledge researchers from the Tokyo Institute of Technology, Soichi Sakurai and Prof. Takashi Tomura from Ando and Hirokawa Antenna Research Group, Japan, for helping us in fabrication and measurement of the metasurface prototypes.

I am also grateful to the thesis committee, Prof. Derek McNamara, Prof. Tom Smy and Dr. Pavan Gunupudi, for taking the time to attend my thesis defence and for providing me with constructive feedback on my work.

Finally, I wish to express thanks to my husband Saurabh, without his continuous support and understanding, this would not have been possible. I also appreciate my little daughter Naisha for abiding my ignorance and the patience she showed when I was busy during the studies. I am grateful to my parents Shashi and Ravi, and my sister Mani, for their encouragement and for always believing in me. And also, my friends, Chetan, Karan, Raj, Swara, and Utkarsh for making these two years such a memorable and worthwhile experience.

ABSTRACT

Extrapolating from current market trends of rising consumer demand and financial growth in mobile technology, it is predicted that the next generation wireless networks will be required to support about a 1,000-fold increase in data capacity to handle over 100 billion devices featuring peak rates of 10 Gb/s and low data transmission latency. Due to limited and expensive spectrum availability at lower microwave frequencies (up to ≈ 10 GHz), the recent introduction of the 60 GHz mm-wave spectrum (IEEE 802.11ad), can be seen as a first step towards the inevitable transition towards millimeter-wave (mm-wave) technology. Due to atmospheric absorption and scarcity of line-of-sight (LOS) channels in practical radio frequency (RF) environments, the mm-wave communications systems are particularly suited for short-range communication systems. While this limits the range of communication systems, it allows for a high level of frequency re-use and therefore makes it attractive for short-range communication applications in dense urban environments. While this transition may simplify system architectures due to large available spectrum, the current microwave technologies are not directly scalable. Novel technological solutions are needed at mm-wave frequencies, ranging from large bandwidth devices to smart antennas and power-efficient wave propagation through cluttered environments. In this context, this thesis concerns with controlling the propagation characteristics of mm-waves using Electromagnetic (EM) metasurfaces, which are 2D counterparts of more general volumetric metamaterials. Metasurfaces are engineered surfaces which can transform the specified waves to desired wavefronts by using amplitude, phase and polarization transform. These metasurface could be envisioned to be used as standalone devices in various RF environments to control wave propagation, such as increasing RF coverage, for instance, or used in conjunction with antenna sources to beam-form with specific characteristics. Very little work has been done in the area of developing mm-wave metasurfaces so far, particularly in the upcoming IEEE 801.11ad band of 60 GHz. In this work, an all-dielectric implementation of mm-wave metasurfaces is investigated using micro-machining of bulk dielectrics. Huygens' metasurface, as a specific class of metasurface, has been investigated here due to its zero back-scattering property. Compared to the existing Printed Circuit Board (PCB) based designs, the all-dielectric metasurfaces are simple to design, while requiring a non-conventional micro-machining process. Various metasurfaces at 30 GHz are designed and various wave transformation are shown here. To push the limits of the design, a 60 GHz metasurface is designed and fabricated to achieve a beam-broadening operation. While encouraging results are obtained, it is found that the micro-machining process at these frequencies is susceptible to large but predictable fabrication tolerances.

TABLE OF CONTENTS

ACKNOWLEDGEMENTS	iii
ABSTRACT	iv
TABLE OF CONTENTS	v
LIST OF FIGURES	vii
Chapter 1 Background & Motivation	1
1.1 5G and Transition to Millimeter-Waves	1
1.2 Application Examples	1
1.3 Thesis Contribution & Organization	3
Chapter 2 Metasurfaces as Beam-forming Elements	5
2.1 Electromagnetic Metasurfaces	5
2.2 Generalized Snell's Refraction - An Example of Wave Manipulation	8
2.3 Metasurfaces as Antenna Beam-formers	10
2.4 Huygens' Metasurface & their Typical Implementations	12
Chapter 3 Metasurface Design Procedure	16
3.1 Numerical Simulation Setup	16
3.2 All-dielectric Unit-Cell Model	17
3.3 Beam-forming using Metasurfaces	20
Chapter 4 Metasurface Demonstration	29
4.1 All-dielectric Metasurface Design	29
4.2 Experimental Demonstration	31
Chapter 5 Summary & Future Works	37

5.1 Key Conclusions	37
5.2 Future Works	38
Bibliography	40

LIST OF FIGURES

Figure 2.1	Generalized Snell’s Law, induced by a phase gradient ϕ_g at an interface.	9
Figure 2.2	Application of metasurfaces for antenna beam-forming.	11
Figure 2.3	Example of a wave refraction when using metasurface as a phase plate. a) Field amplitude and phase just above the metasurface, and b) The far-field pattern obtained using Eq. 2.6.	12
Figure 2.4	Typical Huygens’ unit cell configurations. a) Unit cell at optical frequencies, where a high permittivity dielectric (usually Silicon) is fabricated on top of low permittivity dielectric (such as Silica) [1], b) Microwave implementation of all-dielectric metasurface using laser engraved dielectrics [2]. c-d) Typical PCB based multilayer configurations operating in the microwave frequency ranges [3], [4].	14
Figure 3.1	Numerical model of an all-dielectric Huygens’ unit cell. a) An ideal cell consisting of a high permittivity puck embedded in air. b) Dielectric puck with bridge interconnections for mechanical support. c) An elliptical shaped unit cell with increased degree of freedom. d) A reduced numerical model based on quarter unit cell exploiting the cell symmetry. Various boundary conditions are shown as well and the wave propagation is along the z -direction.	19
Figure 3.2	Typical S-Parameter response of an all-dielectric Huygens’ unit cell of Fig. 3.1, showing the transmission/reflection magnitudes and the transmission phase for two configurations when a) the electric and magnetic resonances occur at two different frequencies, and when b) the electric and magnetic resonances occur at the same frequency.	20
Figure 3.3	FEM-HFSS response of a Huygens’ unit cell for varying geometrical parameters to achieve a 2π phase coverage while maintaining a good matching. a) S_{11} for all several unit cells with matching well below -10 dB, and b) the corresponding transmission phase response.	21
Figure 3.4	Numerical model of a finite size Huygens’ metasurface built in HFSS. Metasurface is assumed to be uniform along the x -axis but exhibits varying transmission response along the y -axis for faster computation.	21

Figure 3.5	FEM-HFSS field results of a uniform metasurface for beam broadening. a) Reflection response. b) Near-field phase profile at $z_0 = 2.5$ mm. c) Co-polarized radiation pattern ($E_\phi(\theta)$ at $\phi = 90^\circ$) at the design frequency of 31.5 GHz, and d) at two neighboring frequencies. The design parameters are: $\tau = 1.07$, $w = 0.58$ mm, $R_{\text{out}} = 1.67$ mm. The dielectric material used is RO3006, with permittivity 6.5 and loss tangent of 0.002 and thickness of 100 mils.	23
Figure 3.6	FEM-HFSS field results of a generalized refraction metasurface for beam broadening. a) Reflection response. b) Near-field phase profile at $z_0 = 30$ mm. c) Co-polarized radiation pattern ($E_\phi(\theta)$ at $\phi = 90^\circ$) at the design frequency of 31.5 GHz, and d) at two neighboring frequencies.	24
Figure 3.7	FEM-HFSS field results of a Difference-pattern metasurface for beam broadening. a) Reflection response. b) Near-field phase profile at $z_0 = 10$ mm (measured from the metasurface). c) Co-polarized radiation pattern ($E_\phi(\theta)$ at $\phi = 90^\circ$) at the design frequency of 31.5 GHz, and d) at two neighboring frequencies.	25
Figure 3.8	FEM-HFSS field results of a Lens metasurface for beam broadening. a) Reflection response. b) Near-field phase profile at $z_0 = 40$ mm. c) Co-polarized radiation pattern ($E_\phi(\theta)$ at $\phi = 90^\circ$) at the design frequency of 31.5 GHz, and d) at two neighboring frequencies.	27
Figure 4.1	The unit cell library used for constructing an all-dielectric metasurface obtained using HFSS. a) Variation of the transmission phase coverage with varying unit cell parameters. b) Relationship between the puck radius and the bridge thickness with the puck ellipticity for several set of matched unit cells. c) Mapping between transmission phase and puck ellipticity at 61 GHz.	30
Figure 4.2	Near-field phase distributions and far-field radiation patterns (normalized) of the designed concave lens at the design frequency of 61 GHz along with two neighboring frequencies.	31
Figure 4.3	All-dielectric metasurface prototype. a) Picture of the fabricated 16×16 metasurface of Fig. 4.2. b) Measurement technique.	32
Figure 4.4	Far-field radiation patterns (normalized) obtained from measured near-field response of the metasurface of Fig. 4.3 at three different frequencies, compared with that of slot antenna and FEM-HFSS.	33

Figure 4.5	Pictures of the metasurface using a microscope to estimate the dimensional tolerances and other fabrication non-idealities.	34
Figure 4.6	Modified HFSS model of the metasurface incorporating the rounded edges, period variation and the over-cutting of the puck.	35

Chapter 1 Background & Motivation

1.1 5G and Transition to Millimeter-Waves

Extrapolating from current market trends of rising consumer demand and financial growth in mobile technology, it is predicted that the next generation wireless networks will be required to support about a 1,000-fold increase in data capacity to handle over 100 billion devices featuring peak rates of 10 Gb/s and low data transmission latency. The next 5th mobile generation (5G) standards, compatible with these ever-rising demands, are expected to be established around 2019/2020 and deployment of 5G networks should be deployed between 2020/2030 [5]. Due to limited and expensive spectrum availability at lower microwave frequencies (up to ≈ 10 GHz), the recent introduction of the 60 GHz mm-wave spectrum (IEEE 802.11ad), can be seen as a first step towards the inevitable transition towards millimeter-wave (mm-wave) technology.

While this transition may simplify system architectures due to large available spectrum, there are several practical challenges at these bands including 60 GHz [6][7]: 1) higher absorption and propagation loss through oxygen and humid conditions, such as during rain and snow, 2) higher intrinsic device noise because of a large bandwidth of 2 GHz per channel, 3) Scarcity of line-of-sight (LOS) channels in practical radio frequency (RF) environments. and 4) Low space diversity due to directive radiation. While this limits the range of communication systems, it allows for a high level of frequency re-use and therefore makes it attractive for short-range communication (typically less than 1 Km for a 60 GHz system) applications in dense urban environments. Addressing these challenging propagation characteristics, novel mm-wave technological solutions are required to optimize power-efficient wave propagation through such environments.

1.2 Application Examples

Let us consider two specific application examples for future communication systems at the millimeter waves:

(1) *Diffraction Engineered Radio Frequency Environments*: A typical wireless communication network can operate in two distinct wireless frequency regimes with two fundamentally different characteristics: a) *Microwave Communication*: At microwave frequencies ($\approx < 10$ GHz), the Electromagnetic (EM) wave interaction with the environment is highly diffractive (non-directive) in nature, due to smaller antennas compared to the physical environment and

their operating wavelengths. The strong scattering as a result of quasi-spherical wavefronts emanating from the sources, are reflected off various physical objects within the wireless environment and create multiple paths and signal copies at the intended receivers. This provides rich channel diversity which is then used to recover the useful signal buried inside the noisy non-Line-of-Sight (non-LOS) wireless channel. This is extensively used in typical Multiple Input Multiple Output (MIMO) systems to enhance the quality of signal transmission across devices [8][9]. b) *mm-Wave Communication*: At mm-wave bands, electrically large signal sources are possible, due to smaller wavelengths. This leads to directive signal propagation thereby naturally reducing the channel diversity with a dominant LOS-type communication. While channel diversity is a fundamental characteristic at microwave frequencies for MIMO systems, its greatly reduced at mm-wave bands. This thus greatly restricts the mm-wave propagation inside typical RF environments due to its extreme sensitivity to scattering from various objects, thereby suitable for short-range communication only. Given that the waves naturally propagated in a directive fashion, there is also a unique opportunity to investigate a paradigm shifting approach of engineering and designing the RF environment itself, to dynamically route the EM energy to form the desired and distinct wireless mm-wave signal paths, to increase the coverage and communication distances. In this context, the RF environment can be modified by introducing controlled local reflection/diffraction engineered EM objects in strategically chosen locations within the RF environment, instead of passive reflections and transmissions through physical objects. This requirement of controlled reflection/diffraction is possible using smart physical devices known as *Metasurfaces*. Metasurfaces are 2D counterparts of more general volumetric Metamaterials (MTMs). They are artificial EM scatterers consisting of 2D arrays of *sub-wavelength resonators* to locally control the EM interaction in terms of transmission/reflection magnitudes and phase and polarization [10]. This application thus involves strategic installation of metasurfaces as smart EM objects, at specifically chosen locations to: 1) wirelessly guide and channel the EM energy to desired areas in a given environment, 2) to exploit the wave-diffraction effects resulting from physical obstructions in the environment to enhance the quality and coverage of wireless signal transmission. More specifically, a new type of wireless network can be envisioned using these EM metasurfaces at mm-waves (> 50 GHz bands including IEEE 801.11ad), based on a combination of the naturally directive wave transmission and the wave-steering and shaping capabilities of EM metasurface scatterers, thereby converting an otherwise unstructured scattering environment into a simplified and a deterministic giant wave-guiding system.

(2) *Antenna Beam-forming*: Strategic installation of metasurfaces at specific locations inside a given RF environment also demands novel designs of antenna sources and receivers with enhanced capabilities. While innovative real-time scanning antenna systems with reconfig-

urable beam-forming capabilities are extensively investigated, there is an equally important demand for fixed high-speed wireless systems for short-range communications systems. For instance, a novel Gigabit Access Transponder Equipment (GATE) system has recently been proposed in Japan, for short-range communication system using large antenna arrays operating in their near-fields [11]. Such electrically large arrays produce quasi plane-waves in the near-field region, maintaining their beam widths to several meters, providing a dedicated coverage area with high-speed data bursts for ultrafast data communication. These antennas are typically based on slot arrays using hollow-waveguides which has recently been proved to be an attractive antenna technology at mm-waves due to low dissipation losses, thereby featuring high efficiencies and antenna gain [12, 13, 14]. They are typically corporate-fed slot arrays which can be readily manufactured using novel diffusion-bonded technique [15], thereby completely avoiding any dielectric materials. Various slot configurations have also been explored to achieve various polarization and broadband radiation performances. While they offer superior performances, they are complex to fabricate. Consequently, they have been dominantly restricted so far to uniform field aperture distributions to achieve high gain at broadside only. In various applications including GATE, it is highly desirable to engineer the radiation fields in both near-field and far-field zones, to achieve specified beam-profiles, i.e. antenna beam-forming, for designing wide variety of coverage zones. This can either be achieved by engineering sophisticated antennas or finding a mechanism to engineer the near-fields of the structure. Given the complexities, cost and challenging practical realizations of such large arrays at mm-waves in addition to the already existing and deployed antenna systems, manipulating their near-field using external means becomes an attractive solution. One such approach is cascading mm-Wave antennas with external 2D metasurfaces which are engineered to manipulate the 2D near-fields of the antennas, to transform both their near-fields, as well as the far-fields to achieve desired field characteristics.

1.3 Thesis Contribution & Organization

The core of both these applications is EM metasurfaces. So far very limited work has been done in the development of mm-Wave metasurfaces which has mostly been limited to microwave frequencies simply as a proof-of-concept tool for demonstrating their sophisticated wave transformation capabilities. With upcoming applications in 5G such as the ones described above, novel solutions based on EM metasurface require an active research in design and implementations of high performance and versatile metasurface structures. This is essentially missing in the literature, and thus presents a unique opportunity for innovation in the area of high frequency RF metamaterials. In this thesis, an attempt is made to devise

mm-Wave EM metasurfaces in the context of these above applications achieving specific wave transformations. This is approached by investigating new designs of Huygens' metasurfaces which provide efficient and attractive ways to manipulate EM fields both in reflection as well as transmission. An inspiration has been taken from optical Huygens' metasurfaces which are based on 2D array of dielectric resonators, whose feasibility was recently demonstrated in [2] using a uniform metasurface. In this research, such a dielectric implementation of Huygens' metasurfaces is extended to mm-Waves, with phase engineering capability through non-uniform metasurfaces. A novel elliptically shaped unit cell providing more degrees of freedom is employed to enable various wave transformation possibilities at two strategic 5G bands around 30 GHz and 60 GHz, with an initial prototype developed at 60 GHz showing encouraging results.

This thesis is organized as follows: Chapter 2, provides a brief background on metasurfaces and describes the basic principle of beam-forming when used in conjunction with an antenna array. Chapter 3, describes in details the all-dielectric implementation of the Huygens' metasurface, with recipes for numerical modeling and design, followed by illustrating several beam-forming examples. Chapter 4, describes an initial design of a 60 GHz all-dielectric Huygens' metasurface along with its performance highlighting several challenges and opportunities for future work. Finally, summary and future steps are provided in Chapter 5.

Chapter 2 Metasurfaces as Beam-forming Elements

2.1 Electromagnetic Metasurfaces

Metamaterials [16, 17, 18] have attracted great interest in the last two decades because of their ability to manipulate electromagnetic waves at subwavelength scale which produces fascinating properties such as anomalous refraction and reflection [19], sub-diffraction imaging [20, 21], negative index of refraction [22, 23], invisible cloaking [24, 25, 26], and other various applications [27, 28, 29], all of which would not be possible to attain in naturally occurring materials using their optical properties. However the use of metallic structures and bulkiness associated with them, high losses and strong dispersion due to the resonant response and problems in fabricating these volume metamaterials have inhibited their practical applications [30].

The 2-dimensional version of metamaterials are known as metasurfaces. These metasurfaces are made of two-dimensional periodic structures of sub-wavelength scattering particles, engineered in a way that they are capable of transforming incident waves into desired reflected and refracted waves [31]. Metasurfaces have been playing such an important role in both optics and microwaves because of many reasons. One is the ease of fabrication being lighter over their 3-D counterpart metamaterials. Secondly, they suffer less from dissipation losses because of the reduced dimensions. The phase, amplitude and polarization of light can be effectively manipulated using engineered metasurfaces [32, 33].

Due to the recent advances in the field of metasurfaces which are nothing but planar metamaterial structures, it has become widely understood that a deeper control of electromagnetic waves can be achieved by the designs that include sub-wavelengths since they possess both electric and magnetic polarizations and also they allow full manipulation on reflected and transmitted waves. Different structures and specific features of the sub-wavelength elements these metasurfaces consist of, defines the electromagnetic properties and functionalities of metasurfaces. Various exotic effects have been exploited to increase the wave transformation capabilities of metasurfaces, such as for example the Pancharatnam effect. Hasman and co-workers carried out a very innovative piece of research which was the use of concept of Pancharatnam-Berry phase or the Geometric phase [34] [35] [36]. The phase change it involved was because of the varying optical polarization. This work was the key step in the development of metasurfaces. The frequency independent phase modification of a transmitted wave is the characteristic of Pancharatnam-Berry phase and operating principle of the same can be described by Jones matrices [37]. There have been many demonstrations based

on Pancharatnam Phase in the past and still continue to happen. For example in 2017, in [38], they created the thinnest metasurface for visible color hologram in transmission mode using the same concept. Metasurfaces have found enormous potential applications such as but not limited to: wave bending [39, 40, 41], holography [42], wave plates [43], perfect absorbers [44, 45], polarization rotation [33, 46], flat lensing [47], harvesters [48], fluid controllable surfaces for tuning and sensing [49], reflectarrays [50, 51] etc to name a few. A good review on the recent developments in metasurfaces analysis and their potential applications can be found in [52].

These 2-D counterparts of metamaterials can be implemented easily from microwaves to optical frequencies because of their flat geometry and simplified fabrication process over the bulky 3-D metamaterials. The reduced thickness (much smaller than wavelength) can significantly lower the undesirable losses by using the suitable material which is difficult to achieve with conventional optical devices [32].

In the optical regime, most of the metasurface research has been done using sub-wavelength plasmonic structures. These metasurfaces consist of metallic nanoparticles structures and substrates which has the ability to control attributes of light [53, 54]. Typical plasmonic implementation involves Silicon/Silicon nitride etc based structures on a dielectric substrate to provide good mechanical support. An example of beam steering using a Silicon based dielectric metasurface is demonstrated in [55]. However, these structures are plagued by losses owing to their metallic nature. The drawback with plasmonic structures is that the light energy is dissipated in the form of heat energy thus witnessing a reduction in efficiency in manipulating an incoming beam for the complete control of polarization and phase [56] [57]. To overcome these limitations, all-dielectric metasurfaces have gained more popularity. Dielectric unit cells are typically comprised of dielectric cylinders of circular cross-section having certain permittivity embedded on a substrate with different permittivity. The basic idea is to have both electric and magnetic resonances overlapped by tuning the physical parameters of the dielectric resonator in order to achieve 2π phase control [58]. Some of the all-dielectric implementation in optical regime is shown in [59, 60, 61, 62].

All the mobile technology and satellite communication is based on the microwave frequency range. It is also the basis of radar technology, applications in imaging and non-contact sensing etc. Thus, having the ability to manipulate waves at this frequency range becomes of practical importance. The concept of transmit-arrays (to replace lenses) and reflect-arrays (to replace reflectors) have been widely used in microwaves frequencies [63, 64, 65] using Printed Circuit Board (PCB) technology. The gist of reflect-arrays is the use of antenna concept that integrates the array advantages with that of a simple reflector to achieve 2π

phase coverage [66]. Frequency selective surfaces (FSS) [67] have also been very popular in microwaves which are used for frequency filtering. FSS usually involves dielectric substrate with periodically arranged metal elements on top [32].

Metasurfaces can be implemented depending on the frequency range and what polarization properties the metasurface should have to perform a certain way. At radio frequencies which include both microwaves (1-30 GHz) and millimeter waves (30-300 GHz), metasurfaces can be implemented as either PCB structures or the all-dielectric ones. Majority of metasurfaces have been demonstrated as PCB structures only due to readily available mature fabrication processes. At higher frequencies like millimeter waves, these PCB structures are challenging due to fabrication and tolerance requirements. Sophisticated wave transformations, particularly in transmission, requires multi-layer configurations, which becomes costly, complex and susceptible to tolerances. Tolerances are also very high at higher frequencies thereby making the PCB technology not very suitable and alternatives are explored such pure all-dielectric structures. Consequently, all-dielectric implementations inspired from optical metasurfaces structure are also gaining attraction because of low losses and fabrication feasibility [2]. In comparison to their metallic counterparts [62, 68, 69], all-dielectric metasurfaces [70, 71] are advantageous because of lower ohmic losses [61].

mm-Waves waves have been identified as a potential candidate for solving a plethora of problems in wireless communication and data transfer for example- in wireless 5G communication which will require large bandwidth and ultra-high data transfer rates, connected homes, cloud connected devices, sensors, satellite tracking etc. Millimeter waves frequencies have the ability to carry massive amounts of data at very high speed and reliability which makes them ideal for fulfilling the new 5G connectivity demands [72]. At these high frequencies, antennas have high transmission losses and in order to prevent this, metasurfaces have been extensively studied and given attention to in order to improve antenna performance.

In 2013, transmit-arrays were designed and fabricated in [73] at mm-wave wave frequencies, precisely at 77 GHz. Those were used for phase and polarization control. Since the PCB fabrication has its own limitations and high tolerances, the design becomes very challenging. A novel metasurface was presented at 28 GHz of frequency [74]. It was composed of unit cells working as spatial filters having different phase shifts depending upon the polarization of the incident beams in addition to having passband characteristics. The unit cell [75, 76] is made of layers of dielectric with metallic patches on top and bottom and a metallic grid in between the dielectrics. The use of metals and multilayer structure makes it complicated to fabricate and more prone to losses. A dielectric reflect-array based on linearly polarized mm-wave substrate was fabricated on PCB [77] in the frequency range from 30 to 40 GHz. The unit cell they have

shown has four arms in order to avoid the alignment problems. This metasurface is limited to reflection and PCB fabrication was reported to be very challenging. As another example, [78] shows an anisotropic coding based metasurface at 60 GHz. The unit cell consists of metallic layers and the dielectric substrates sandwiched between each other. The use of multilayer although provides flexibility, comes with complicated fabrication process and large losses. These works demonstrate that there is a need to explore novel metasurface designs at the mm-Wave frequency ranges to achieve more richer and wide variety of wave transformations, and devise new fabrication processes suitable for high-performance mm-wave metasurfaces.

2.2 Generalized Snell's Refraction - An Example of Wave Manipulation

The very well known Snell's Law which describes the relationship between angle of incidence and angle of refraction across a dielectric-dielectric interface, states that the refraction index for the slower medium times the sine of the angle of refraction is equivalent to the refractive index of the first medium times the sine of the angle of the incidence.

$$n_2 \sin \theta_r = n_1 \sin \theta_i \quad (2.1)$$

where n_2 = refractive index of medium 2, n_1 = refractive index of medium 1, θ_r = angle of refraction and θ_i = angle of incidence.

If conceptually, we place an array of sub-wavelengths antennas on the interface between two different media and light incidents on the interface, each antenna, when couples to light, shifts the phase abruptly. If these antennas are different from each other, the shift in phase will be different at various locations which is equivalent to introducing gradient of phase along the interface. That actually results in a very fundamental modification of Snell's law for both reflection and refraction. So this basically explains we could send light in any direction of our will and not just the one dictated by Snell's law. This modification is generally referred to as the Generalized Snell's Law. The generalized Snell's law was first demonstrated by Capasso group in mid infrared wavelengths [19]. If these antennas are not there, the angle of reflection is naturally equal to the angle of incidence through the ratio of refractive indices which is the very popular Snell's law of Eq. 2.1. Generalized Snell's law can be derived by Fermat's Principle which states that the ray of light will propagate in a way that the optical path between source and destination is minimized. It will take the fastest path (and not the most direct) [79]. Alternative approach is to conserve wave momentum across the interface. Let us consider an incident plane wave with an incident angle of θ_1 as shown in Fig. 2.1, which is refracted at an angle of θ_2 in the second medium. A metasurface lying at the interface

is designed to provide a linear phase gradient $\phi_g = d\phi/dx$. Considering that the total wave momentum (transverse wave number) must be continuous across the interface, we get

$$k_0 n_1 \sin \theta_1 + \frac{d\phi}{dx} = k_0 n_2 \sin \theta_2 \quad (2.2)$$

$$\Rightarrow n_2 \sin \theta_2 - n_1 \sin \theta_1 = \frac{\lambda_0}{2\pi} \frac{d\phi}{dx} \quad (2.3)$$

where n_1 and n_2 are the refractive indices of the two media, k_0 is the wave number $k_0 = \frac{2\pi}{\lambda_0}$ and $\lambda_0 =$ free space wavelength. This expression is termed as the Generalized Snell's Law.

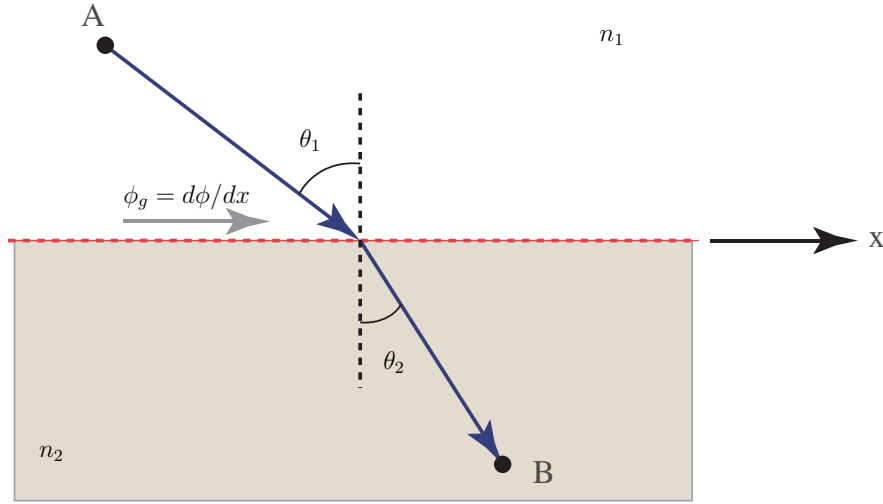


Figure 2.1 Generalized Snell's Law, induced by a phase gradient ϕ_g at an interface.

We can thus conclude that if we are able to engineer suitable constant phase gradient discontinuity $\left(\frac{d\Phi}{dx}\right)$ along the interface, the refracted beam can be bend in a desired direction.

In case where this phase gradient discontinuity becomes zero $\left(\frac{d\Phi}{dx} = 0\right)$, we get the normal Snell's law where the angle of incidence will be equal to the angle of refraction [80].

Therefore, we can say that we could send the light in desired direction depending on our metasurface design. It basically shows how fundamentally we change the way light propagates through a medium. If we have control over the phase, we have full control over the light propagation with structures that are much smaller than the wavelength. There are many groups all over the world who have demonstrated various developments in this field using phase control for example optical holography [81], broadband light bending [39], ultra thin plasmonic metalens [82, 83], meta-holograms [84, 85, 86, 87], metasurface holograms for

visible light [88], beam steering and shaping [89] etc.

2.3 Metasurfaces as Antenna Beam-formers

While metasurfaces are wave transformation elements, and are typically used/tested as stand-alone devices operating on specified waves, they can alternatively be seen as directly modifying the source fields, which in radio-frequencies are typically generated using *Antennas*. In the application context of GATE application, for instance, to achieve the desired radiated fields from large antenna arrays, either the antenna itself could be synthesized to produce those fields in the near or far-fields, or the source fields are indirectly modified and transformed using metasurfaces as external elements. At mm-Waves specially, considering the implementation and design complexities, particularly related to the slot array antenna designs using the diffusion bonding process, creating non-uniform aperture for complex wave-front shapes is an extremely challenging task. Moreover, often times, it is not possible to replace pre-existing antenna installations by newer designs due to cost and deployments related issues. In such cases, using a metasurface to modify the radiated fields of an antenna starts to become interesting and a viable approach. Finally, given practical constraints on space, modifying the aperture fields directly in the near-field of the antenna is the preferred approach to manipulate and obtain the desired fields in the near and far-field regions of the antenna.

The wave-shaping principle of the aperture fields of a 2D antenna is illustrated in Fig. 2.2. Consider a 2D antenna (typically a 2D array of slot antennas) radiating a uniform field on top of the antenna aperture. This field is considered as a source field that we wish to shape directly in the near-field. It is assumed that no control over this field exists and wave-shaping has to be done using purely external means, such as a metasurface operating in the near-field of the antenna. Since the antenna should not be loaded by the metasurface, it must exhibit some key characteristics. It must be matched to incident wave emanating from the antenna, so that minimal reflection exists, which otherwise may be coupled back to the antenna affecting its matching response. Secondly, the metasurface should be broadband to accommodate large mm-Wave bandwidths.

Under these conditions, we seek a metasurface which can achieve a large matching bandwidth, while providing control on the transmission phase and amplitude. For simplicity, we consider only a phase transformation so that the metasurface essentially acts as an all-pass structure, i.e. a phase plate. By controlling the spatial variation of the transmission phase across the antenna aperture, various beam-shaping capabilities are enabled which eventually can be used for far-field beam shaping. To illustrate this operation, assume a uniform plane-

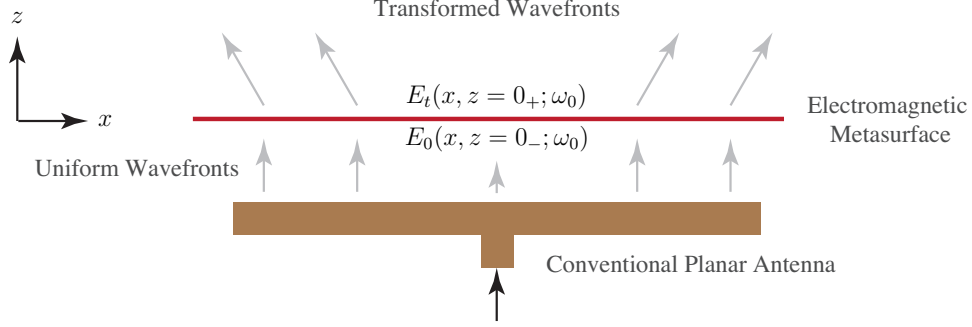


Figure 2.2 Application of metasurfaces for antenna beam-forming.

wave distribution on the top of the antenna at a design frequency ω_0 , and just below the metasurface (incident side), which is then modified by the phase profile of the metasurface. The total fields at the output of the metasurface (above the surface), is then given by

$$E_t(x, z = 0_+; \omega_0) = E_0(x, z = 0_-; \omega_0)e^{j\phi(x)} = e^{j\phi(x)} \quad (2.4)$$

where $\phi(x)$ is phase distribution function across the aperture (1D variation is assumed for simplicity). The radiation pattern of the antenna can be approximated by the Fourier transform of the total field, given by

$$\tilde{E}_x(k_x) = \mathcal{F}[e^{j\phi(x)}], \quad (2.5)$$

with k_x as the spatial frequency. The spatial frequency is then related to the physical angle of radiation in space as:

$$\theta_{rad}(\omega) = \sin^{-1} \left(\frac{k_x}{k_0} \right). \quad (2.6)$$

This thus provides a far-field distribution which could for instance, define the overall goal of the design. We can take the example of wave refraction based on the principle which we described in the previous section, as a perfect demonstration of using metasurface as a phase plate. Let us assume that the phase gradient along the metasurface is $2\pi/L$ where $L = 67.84$ mm (practical design) with unity transmission as shown in Fig. 2.3(a). Following Eq. 2.3, we expect the refraction angle to be 4.16° at $f = 61.5$ GHz. Next, computing the radiation pattern using Eq. 2.6, we get the pattern of Fig. 2.3(b), and as expected, a desired beam refraction is observed following the prediction of generalized refraction. This simple procedure thus illustrates the operation of the phase plate in antenna beam-forming in the

far-field of the antenna. Our next task, is to find a physical metasurface structure providing engineerable phase responses at mm-Waves.

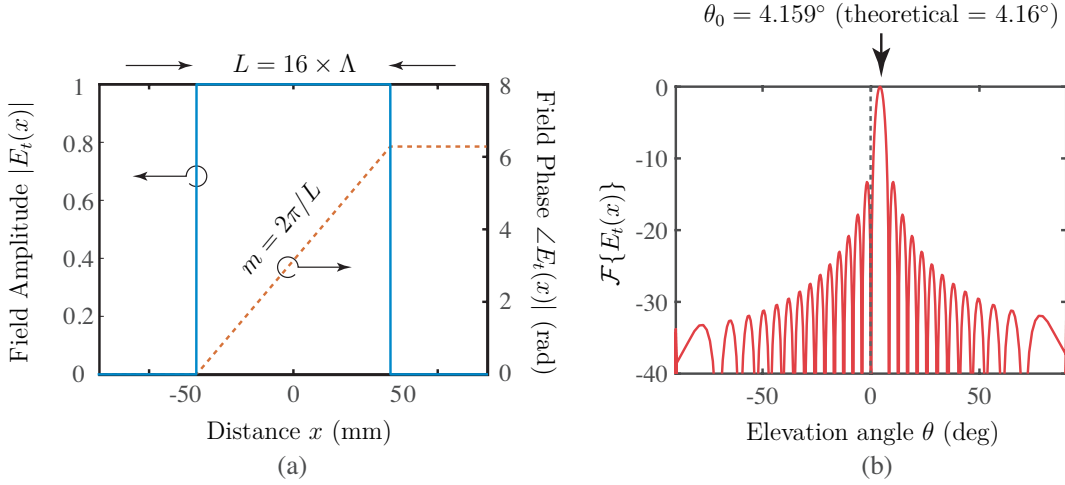


Figure 2.3 Example of a wave refraction when using metasurface as a phase plate. a) Field amplitude and phase just above the metasurface, and b) The far-field pattern obtained using Eq. 2.6.

2.4 Huygens' Metasurface & their Typical Implementations

An interesting class of metasurfaces is of Huygens' metasurface. Huygens' metasurfaces are special class of metasurfaces that generate orthogonal electric and magnetic dipole resonances [90, 91] where these currents act like Huygen's sources. The interaction between the electric and magnetic resonances result in a constructive interference along one direction, and destructive interference along the opposite direction, i.e. zero back-scattering. Huygens' Metasurfaces are sub-wavelength thin and can manipulate desired field attributes of incoming electromagnetic waves such as magnitude, phase and polarization as a result of their dipolar interactions [1]. These surfaces can be conceptualized using the Schelkunoff's equivalence principle [92], which is the generalization of Huygens' principle. Huygens' Principle states that every point on a wavefront acts as a secondary source of outgoing spherical waves at all times. He assumed light to be a wave. The fundamental laws of reflection and diffraction can easily be explained using Huygens' principle. Later the Huygen's principle revealed that each individual source should be explained as an electrically small antenna in order to obtain purely forward-propagating waves [93]. The two resonances can be tuned in a way that we can achieve a wide range of applications which make them a flexible tool for wavefront manipulation. The most attractive feature of the Huygens' metasurface is its excellent matching characteristic in a large bandwidth, which is what we ideally need for them to be used as

phase plates. Broadband Huygens' metasurfaces are thus useful to obtain frequency selective response remaining transparent at other frequencies [94].

A small dielectric resonator sphere or a puck, naturally produces the Huygens' configuration. This simplicity is exploited at optics where coupled dielectric resonators exhibiting constructive interference of their electric and magnetic responses, lead to an all-pass response [95]. A finite size metasurface is thus formed by forming a 2D array of dielectric resonators (quasi-periodic structure), whose geometrical dimensions are varied across the metasurface to realize a given space-varying phase distribution profile required for a desired wave transformation. The finiteness of the unit cell thus discretizes and samples a desired continuous phase profile. Due to this spatial discretization, care must be taken where the unit cell size must be smaller than the wavelength of operation to ensure only fundamental diffraction order exists. This can be understood using the following argument applied to a periodic structure. Consider the metasurface of Fig. 2.2 assumed to be infinitely periodic along the x -direction, with a periodic unit cell of size Λ_x . The EM fields scattered from the metasurface (in the transmission region, for instance in $z > 0$), will also be periodic. They can thus be expanded in terms of Fourier series as

$$\mathbf{E}_t(x, z = 0_+) = \sum_{n=-\infty}^{\infty} a_n e^{-jn k_x x}, \quad (2.7)$$

where $k_x = 2\pi/\Lambda_x$. Each of the terms in the Fourier series represents a plane-wave propagating at an angle θ_n corresponding to the n^{th} diffraction order, which is given by

$$\theta_n = \sin^{-1} \left\{ \frac{n k_x}{k_0} \right\}, \quad (2.8)$$

where the angle θ_n is measured from the normal of the metasurface interface. For propagation angle to be physical and representing a propagating wave, the argument of inverse sin should be less than 1, so that

$$n \left(\frac{2\pi}{\Lambda_x} \right) < k_0 \Rightarrow n < \left(\frac{\Lambda_x}{\lambda_0} \right). \quad (2.9)$$

Finally, if only the fundamental diffraction order is desired, then $\Lambda_x < \lambda_0$, so that only

$n = 0$ (fundamental order) is allowed to propagate. This thus explains the choice of a sub-wavelength unit cell used in metasurface simulations.

A typical all-dielectric metasurface at optics is shown in Fig.2.4(a). For example, in [96], they have demonstrated a gradient Huygens' metasurface with anomalous refraction in wavelengths ranging from ultraviolet to infrared. The technique here is to use the low aspect ratio nano-cylinders to control the phase of the incident wave and achieve a full 2π phase coverage. These nano-cylinders make the use of spectrally overlapped electric and magnetic dipole Mie-type resonances [1, 97]. Similar implementation operating in both transmission and reflection modes have been reported at various optical frequency bands [98, 99]. At RF, the Huygens' metasurface implementation has been mostly using printed metallic structures, such as the ones shown in Fig. 2.4(c-d) based on an asymmetric three-layer PCB unit cell. These unit cells were cascaded to form the metasurface to couple the incident plane wave to a transmitted plane wave at a certain angle. Generally these cells are designed in such a way to introduce different phases corresponding to each unit cell while also maintaining the impedance matching [100].

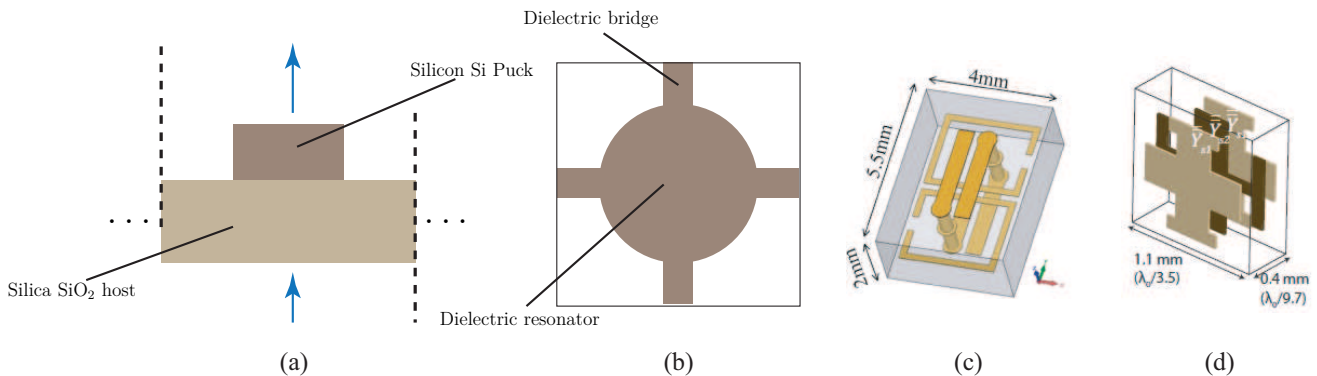


Figure 2.4 Typical Huygens' unit cell configurations. a) Unit cell at optical frequencies, where a high permittivity dielectric (usually Silicon) is fabricated on top of low permittivity dielectric (such as Silica) [1], b) Microwave implementation of all-dielectric metasurface using laser engraved dielectrics [2]. c-d) Typical PCB based multilayer configurations operating in the microwave frequency ranges [3], [4].

RF Metasurfaces are thus typically constructed using metal structures and very limited work has been done in all-dielectric implementation of Huygens' metasurface. In case of metallic structures, complicated geometries have to be devised to achieve an electrically small, orthogonally co-located electric and dipole resonators. Considering the challenges involved in metallic Huygens' surfaces in terms of geometrical complexities and multilayer configurations, along with anticipated fabrication challenges related to narrow line width and gaps at mm-waves, these all-dielectric metasurfaces were first introduced at microwave

frequencies as an alternative approach, using the unit cell of Fig. 2.4(b) [2]. They were fabricated using a novel laser-drilling process by engraving a bulk dielectric slab, where its good matching properties were demonstrated using a uniform metasurface only. While the conventional PCB based Huygens' cells are compact and thin, the all-dielectric unit cells are typically large ($\lambda_0/2 \lesssim \Lambda \lesssim \lambda_0$) and relatively thick ($\lambda_0/6 \lesssim h \lesssim \lambda_0/4$) in comparison¹. While this may be seen as a drawback since due to larger unit cell dimensions, the spatial phase discretization is coarse, it may actually favor reducing fabrication tolerances at higher frequencies.

With this background, the all-dielectric implementation of Huygens' metasurface will be explored and extended to mm-wave frequencies in this thesis. This requires an investigation into devising a flexible unit cell model capable of achieving a 2π phase coverage at a design frequency while maintaining a good match. There is also a related challenge of practically implementing them at high frequencies, where non-PCB based fabrication processes must be experimented while working with small dimensions of the unit cells. Thus an effort is made here to open new directions and techniques to realize mm-wave all-dielectric metasurfaces, and estimate their feasibilities and establish practical limitations. Although, metasurfaces are interesting as stand-alone devices by themselves, their capability to operate in the near-fields of the antennas is also of particular interest in the context of mm-wave beam-forming applications.

¹At such relatively large thicknesses, all-dielectric structures start to look like bulk 3D structures, rather than *surfaces*, so that calling them a surface becomes questionable. We will continue to refer them as metasurfaces here to be consistent with literature and the fact that their scattering properties can still be accurately modeled using a zero-thickness sheet. However, caution must be taken in this terminology.

Chapter 3 Metasurface Design Procedure

A physical metasurface is a 2D array of sub-wavelength resonators forming a surface, whose individual scattering responses are engineered to create a desired macroscopic effect. The resonator thus forms the building block of the metasurface and is referred to as the unit cell. In this chapter, the metasurface design procedure is described in details using the all-dielectric unit cell as the representative example.

3.1 Numerical Simulation Setup

The electromagnetic behavior of the proposed structure is studied in Ansys High Frequency Structure Software (HFSS) based on the Finite Element Method (FEM). Majority of the work carried out in this thesis is designed and evaluated in HFSS. It is a full 3D Computer Aided Design (CAD) tool that allows us to create various physical models using different materials, geometries and boundaries. HFSS uses finite element method (FEM) to compute electromagnetic behavior of high frequency elements and is a frequency domain method.

For achieving a desired wave transformation at a given frequency, where the specified incident fields are transformed into desired scattered fields (reflection and transmission), the metasurface is first synthesized in terms of surface susceptibility densities across the surface [101]. The general space dependent surface susceptibilities are then related to the local transmission and reflection properties of the surface, in response to plane-wave excitations. Essentially, the surface is described in terms of complex transmission $T(\mathbf{r}, \omega)$ and reflection $R(\mathbf{r}, \omega)$. While these transfer functions are continuous, they are sampled in practical realizations by a discrete array of resonators. Each of these resonators, referred to as the unit cell here, is then simulated and analyzed independently within a periodic environment in HFSS before finally combining again to realize the overall metasurface. The fundamental requirement for metasurface designs is that the sampling period $\Lambda < \lambda_0$. This ensures that only the fundamental diffraction order exists and higher order diffraction beams are completely suppressed. It should be noted that while the rigorous approach for designing metasurface for general wave transformation requires synthesizing surface susceptibilities, the phase profile of the metasurfaces can be easily predicted for simpler wave transformation cases, as will be shown later in this chapter.

An all-dielectric metasurface is essentially a 2D array of small dielectric pucks of specific shape. Let us consider a basic square shaped unit cell consisting of a dielectric puck (circular-

shaped) using a substrate of certain thickness with a hole subtracted from the centre of it, lying in the $x - y$ plane. Using periodic boundary conditions (PBC) in HFSS, it is possible to analyze an infinite structure by using a single unit cell. To apply the periodic boundaries (Floquet boundaries in HFSS), one has to define two surface pair which are Master and Slave in such a manner that the electric field on a master matches the electric field on its corresponding slave with a particular phase difference. This unit cell simulation with Floquet boundaries thus emulates an infinite 2D array, where all neighboring EM coupling are taken into account. To emulate a plane-wave incidence on the unit cell, a phase shift of 0° is imposed on the Slave boundaries. An air box is then added around the unit cell on which the signal ports are next defined. Ports are unique boundaries that allow the energy to flow into and out of the structure. Next, two Floquet ports are defined on each face of the air-box parallel to the metasurface, acting as the source and observation planes.

The shape and the height of the air box play an important role in the simulation set up and the accuracy of the numerical simulation. The air box must be characterized to model open space with the goal that only the propagating fields are captured at the Floquet ports, and all the evanescent fields decay to insignificant contributions at the port locations. This has to be verified by ensuring that as the size of the air-box is changed, the transmission and reflection response remains unchanged. The only way to know that for sure if the HFSS gives us the convergent results is to increase the height of the air box and check the results with the previous results. If the results do not change, it is safe to say that they have converged, and the air-box size is then fixed.

3.2 All-dielectric Unit-Cell Model

Let us design an all-dielectric metasurface around 30 GHz, which is one of the strategic bands of upcoming 5G networks. The all dielectric unit cell consists of a circular puck made with a dielectric substrate of $h = 100$ mils thickness with a dielectric constant of $\epsilon_r = 6.15$ and a loss tangent of 0.002, surrounded by air, as shown in Fig. 3.1(a). The reason for choosing a high permittivity material is that the unit cell is a resonator and we want all EM energy to be localized, stored and trapped. A hole of radius $R_{in} = 25$ mils is subtracted from the centre of the puck of radius. The size of each unit cell is fixed to 8.4 mm which is less than the free-space wavelength at 30 GHz (the reason for this will become clear in the next chapter). Although this circular unit cell is an ideal cell, it is impossible to fabricate since it hangs in the air and there is no mechanical support available to hold them together in order to construct the 2D array of metasurfaces. So this circular unit cell has to be modified as shown in Fig. 3.1(b), where now two mechanical supports are added on each side. Since

the overall structure can also be seen as a perforated dielectric substrate, fabrication using laser drilling process can now be achieved easily. Unlike its optical counterparts, the proposed dielectric unit cell here maintains its inherent all-pass response and does not produce spurious resonances (Fabry-Perot type) since there is no host substrate around the resonator. While the original unit cell of Fig. 3.1(a) is symmetric across x - and y - axis, thereby insensitive to incoming polarization, the unit cell with dielectric bridges only works for a single polarization. The incoming E-field polarization perpendicular to the bridges suffers from minimal field perturbation, and thus the unit cell response is maintained. On the other hand, the field parallel to the bridges sees the full extent of the bridge and is strongly reflected. Thus, while the sole purpose of the bridges is to provide mechanical support, it has important EM consequences.

In order to take full advantage of metasurfaces for beam shaping and phase control, the main challenge arises in the ability to achieve any possible phase shift in the range $[0, 2\pi]$ while also maintaining a perfect matching in a large bandwidth. This typically requires geometrical deformation of the unit cell, which requires introducing more degree of freedom. The unit cell period is typically fixed, and the dimensions of the resonator only are usually changed for practical convenience. To introduce more degrees of freedom, for achieving the $[0, 2\pi]$ phase variation, the unit cell of Fig. 3.1(c) is next modified to an elliptical shape, characterized by an ellipticity parameter τ . Thus the ellipticity τ , puck radius R_{out} , hole radius R_{in} and bridge thickness w represent the various geometrical dimensions which can now be tuned and engineered.

We notice that our chosen unit cell exhibits symmetry with respect to the x - and y - axis, and we are primarily interested in the unit cells response at the normal incidence, we can reduce the full unit cell model with Floquet boundary conditions into a more computationally efficient size which is the quarter sized model using PEC and PMC boundaries. Perfect Electric Conductor (PEC) is analogous to a short circuit with zero tangential E-fields, while Perfect magnetic conductors (PMCs) are considered analogous to an open circuit with zero tangential H-Fields [102]. Thus a reduced unit cell model can be devised where only a quarter of the cell is used, the Floquet boundaries are removed and replaced with appropriate pairs of PEC and PMC boundaries, as shown in Fig. 3.1(d). The Floquet ports are replaced with conventional wave ports. This reduced order model is electromagnetically identical to the full cell and requires less computational power and time for efficient and faster design of the metasurfaces.

Let us next look at the reflection and transmission response of the cell. Fig. 3.2 (a) shows the typical scattering parameters (S_{11} and S_{21}) with a large bandwidth when the unit cell

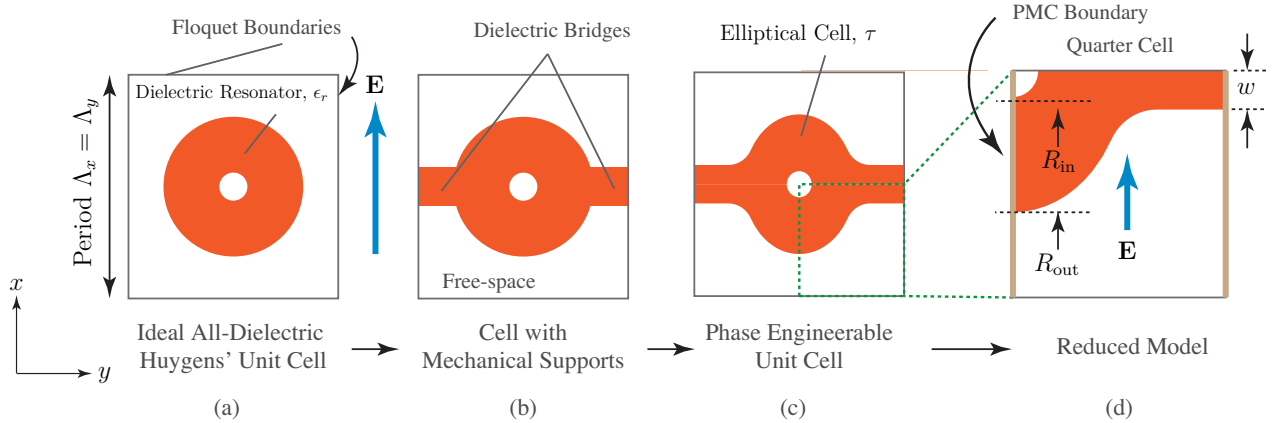


Figure 3.1 Numerical model of an all-dielectric Huygens' unit cell. a) An ideal cell consisting of a high permittivity puck embedded in air. b) Dielectric puck with bridge interconnections for mechanical support. c) An elliptical shaped unit cell with increased degree of freedom. d) A reduced numerical model based on quarter unit cell exploiting the cell symmetry. Various boundary conditions are shown as well and the wave propagation is along the z -direction.

parameters are not carefully optimized. Two sharp transmission dips are observed at specific frequencies, which are associated with electric and magnetic resonance of the structures, where it can be verified that the two resonances are orthogonally polarized. At these resonant frequencies, transmission phase also varies greatly as is expected near the resonance of the structure. Since at any given frequency, only one of the resonances exist, we do not operate the dielectric puck as a Huygens' source, and an overall poor matching (finite back-scattering) is observed.

In order to get broadband matching response, it is important to have the presence of both electric and magnetic dipole resonances at the same frequencies, as required in a Huygens' source. When the unit cell parameters are well optimized, the electric and magnetic resonances start to overlap and we get a good flat transmission across a large band with good matching performance (typically < -10 dB). The two resonances merge, and we form the desired Huygens' source. The corresponding transmission phase response also shows a well-behaved phase profile with inflection point around the resonant frequency of the puck. This clearly indicates a strong frequency dependent phase response with non-linear phase frequency relationship (dispersion). We recall again that this specific response with good broadband matching and non-linear phase is achieved for a very specific set of geometrical parameters of the unit cell.

Next, to design a general wave transforming metasurface, we need to achieve a 2π phase coverage while maintaining matching. So, our objective here is to design a library of unit cells which are all well-matched for a given unit cell size, and providing $[0, 2\pi]$ phase shift

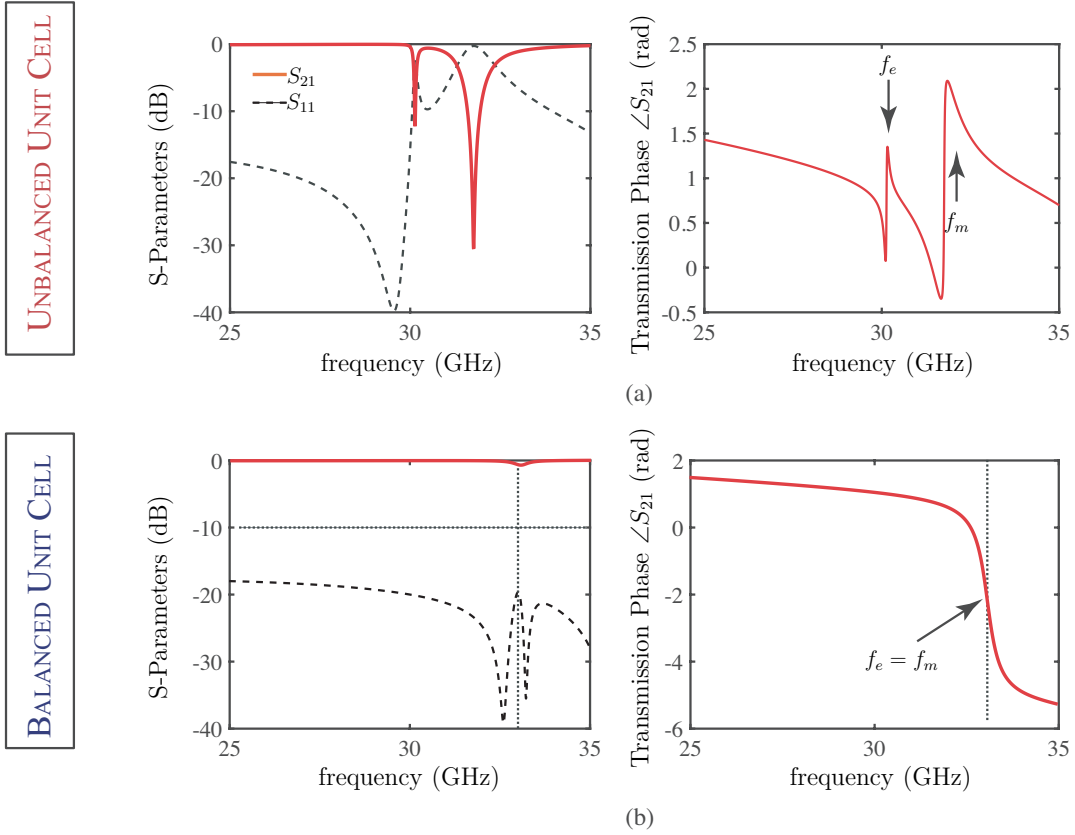


Figure 3.2 Typical S-Parameter response of an all-dielectric Huygens' unit cell of Fig. 3.1, showing the transmission/reflection magnitudes and the transmission phase for two configurations when a) the electric and magnetic resonances occur at two different frequencies, and when b) the electric and magnetic resonances occur at the same frequency.

range at the design frequency while maintaining an all-pass response for a band of frequencies. Fig. 3.3 shows the transmission reflection response of the unit cell of various combinations its geometrical parameters (primarily τ , R_{out} and w). The total phase range, as we can see in the figure is very close to 2π and all the unit cells are well matched since the reflection for all individual cells is less than -10 dB. Therefore, this unit cell is capable of providing an engineerable transmission phase while maintaining good matching in a large bandwidth. This library will be next used to build our overall metasurface.

3.3 Beam-forming using Metasurfaces

Once the unit cell has been engineered, it is arranged in a 2D array to form the overall metasurface. Here we consider a 10×10 metasurface. Given that the unit cell size is sub-wavelength but the overall structure is electrically large, the overall metasurface simulation

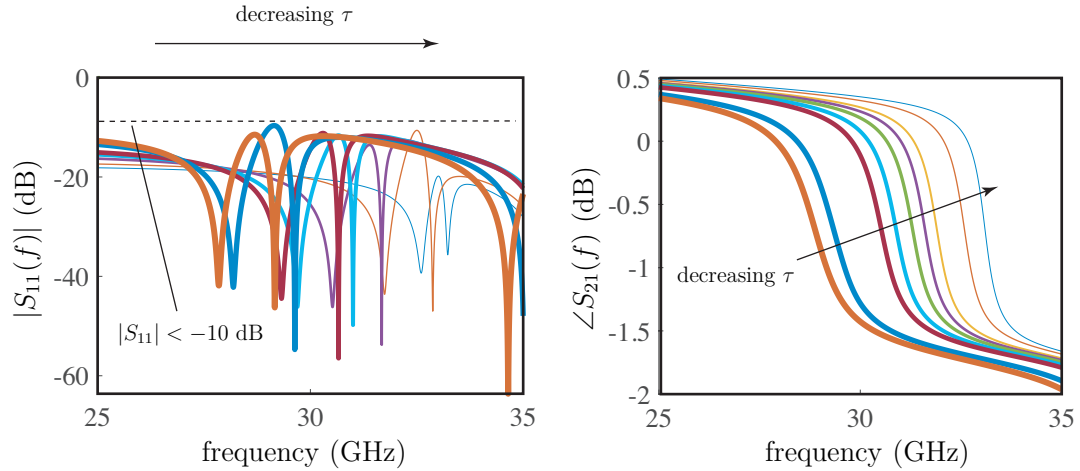


Figure 3.3 FEM-HFSS response of a Huygens' unit cell for varying geometrical parameters to achieve a 2π phase coverage while maintaining a good matching. a) S_{11} for all several unit cells with matching well below -10 dB, and b) the corresponding transmission phase response.

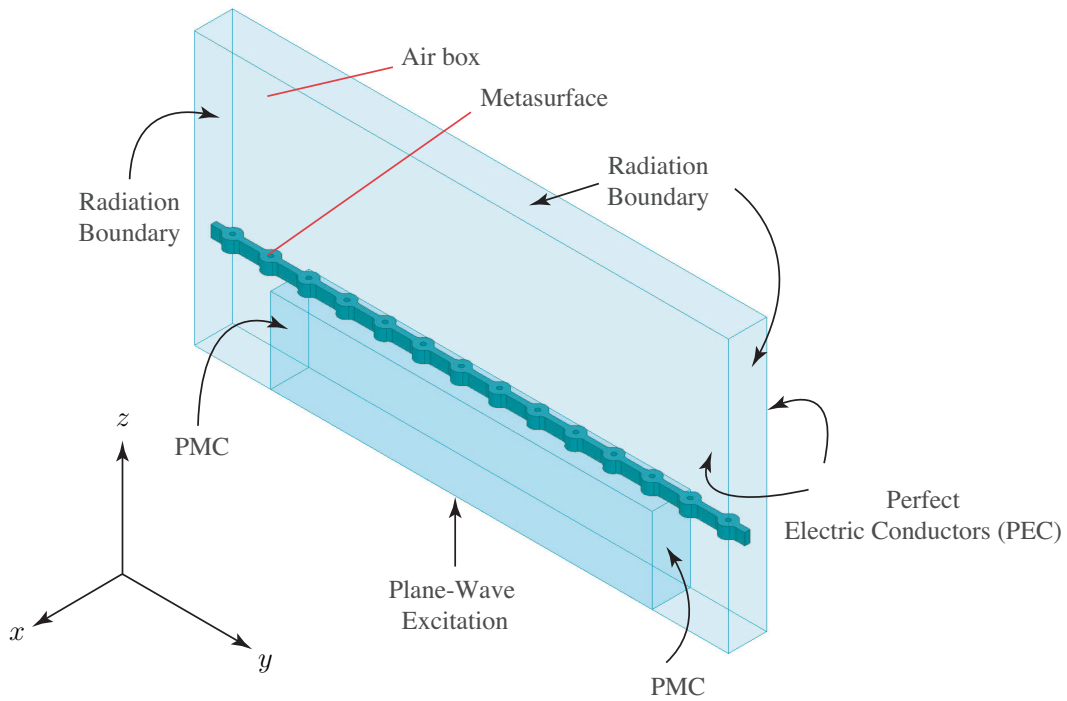


Figure 3.4 Numerical model of a finite size Huygens' metasurface built in HFSS. Metasurface is assumed to be uniform along the x -axis but exhibits varying transmission response along the y -axis for faster computation.

is actually a computationally challenging task, since the numerical simulator has to use fine meshing and apply it to a large computational box. To ease the computational burden, we assume that the metasurface is uniform along one direction, and varies along the other direction only. This allows to construct a less challenging computational model.

Figure 3.4 shows one typical model of 1D array of dielectric pucks indicating various boundaries and port definitions, used in this work. To emulate a finite size extent of the metasurface radiation boundaries are used along one direction, whereas Perfect Electric Conductors (PECs) are applied on the other pair to force no field variation along the x -direction. Finally, since the metasurface is finite sized along y -axis, the edge effects may become dominant resulting in a poor cell response. To reduce the edge effects, two extra unit cells were added on both sides of the metasurface, so that only the middle part of the overall metasurface was illuminated with a plane-wave. The transmission region is terminated with radiation boundaries, which also allows computing the far-field response of the metasurface. Let us next consider various phase configurations of the metasurface to illustrate a variety of beam-forming operations.

1. **Uniform Metasurface:** Before introducing space-varying phase profile on the metasurface, a uniform metasurface is first built and simulated to confirm the simulation model of Fig. 3.4. For this purpose, unit cells of same ellipticities have been arranged periodically in x -direction in order to make the uniform metasurface. Since there is no change in the phase along the metasurface, the wave is supposed to travel straight through the metasurface. This can be confirmed by plotting the far-field radiation pattern of the metasurface. Fig. 3.5(b) and (c) shows the co-polarized radiation patterns at the design frequency (30 GHz) along with few neighboring frequencies. As expected the main lobe is pointed along $\theta = 0^\circ$, with several side-lobe levels indicative of the finite extent of the metasurface. In addition, the narrowing main beamwidth with increasing frequency is also clearly observed.
2. **Generalized Refraction:** Let us introduce a space-variation in the phase by considering an example of a generalized refraction. This requires a linearly increasing (or decreasing) transmission phase as a function of position. Using the unit cell library of the previous section, a close to 2π phase range was designed across the metasurface, as shown in Fig. 3.6. The computed far-field response of the metasurface is shown in Fig. 3.6(b-c) where the refraction (bending) of the beam is clearly seen. The near-field phase response also clearly shows the linear increase in the phase, although exhibiting significant ripples. The observation location of the phase was empirically fixed to obtain a more continuous phase profile, due to phase-wrapping property. The observed refraction angle of 4.16° is found

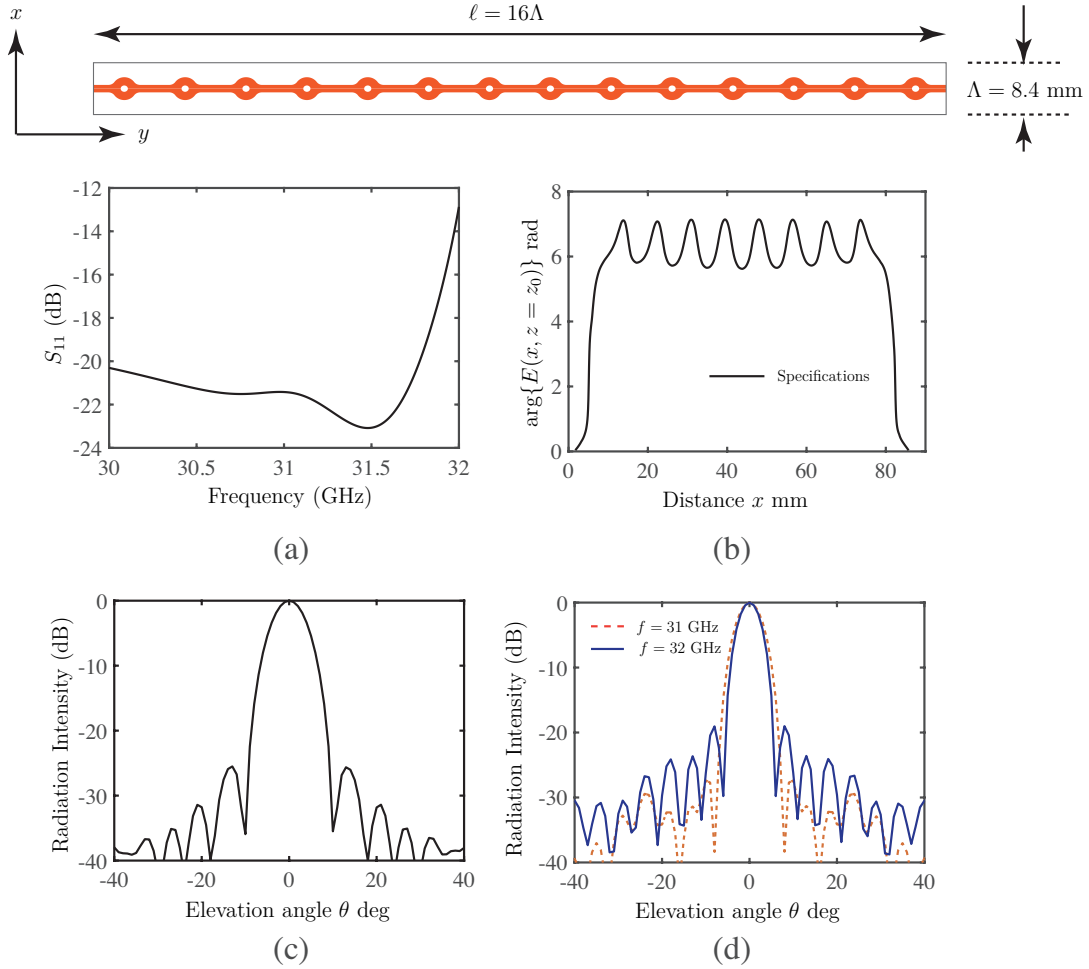


Figure 3.5 FEM-HFSS field results of a uniform metasurface for beam broadening. a) Reflection response. b) Near-field phase profile at $z_0 = 2.5$ mm. c) Co-polarized radiation pattern ($E_\phi(\theta)$ at $\phi = 90^\circ$) at the design frequency of 31.5 GHz, and d) at two neighboring frequencies. The design parameters are: $\tau = 1.07$, $w = 0.58$ mm, $R_{\text{out}} = 1.67$ mm. The dielectric material used is RO3006, with permittivity 6.5 and loss tangent of 0.002 and thickness of 100 mils.

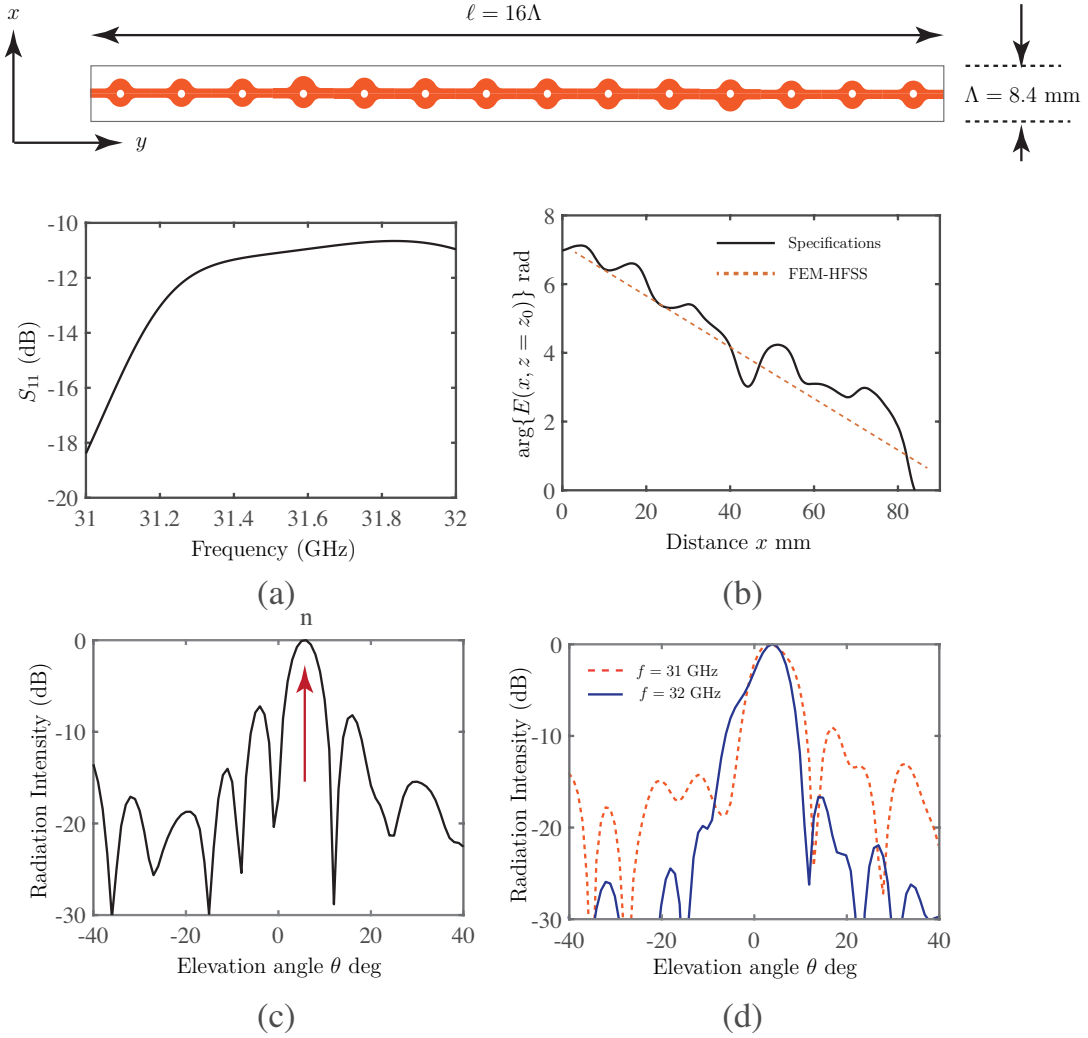


Figure 3.6 FEM-HFSS field results of a generalized refraction metasurface for beam broadening. a) Reflection response. b) Near-field phase profile at $z_0 = 30$ mm. c) Co-polarized radiation pattern ($E_\phi(\theta)$ at $\phi = 90^\circ$) at the design frequency of 31.5 GHz, and d) at two neighboring frequencies.

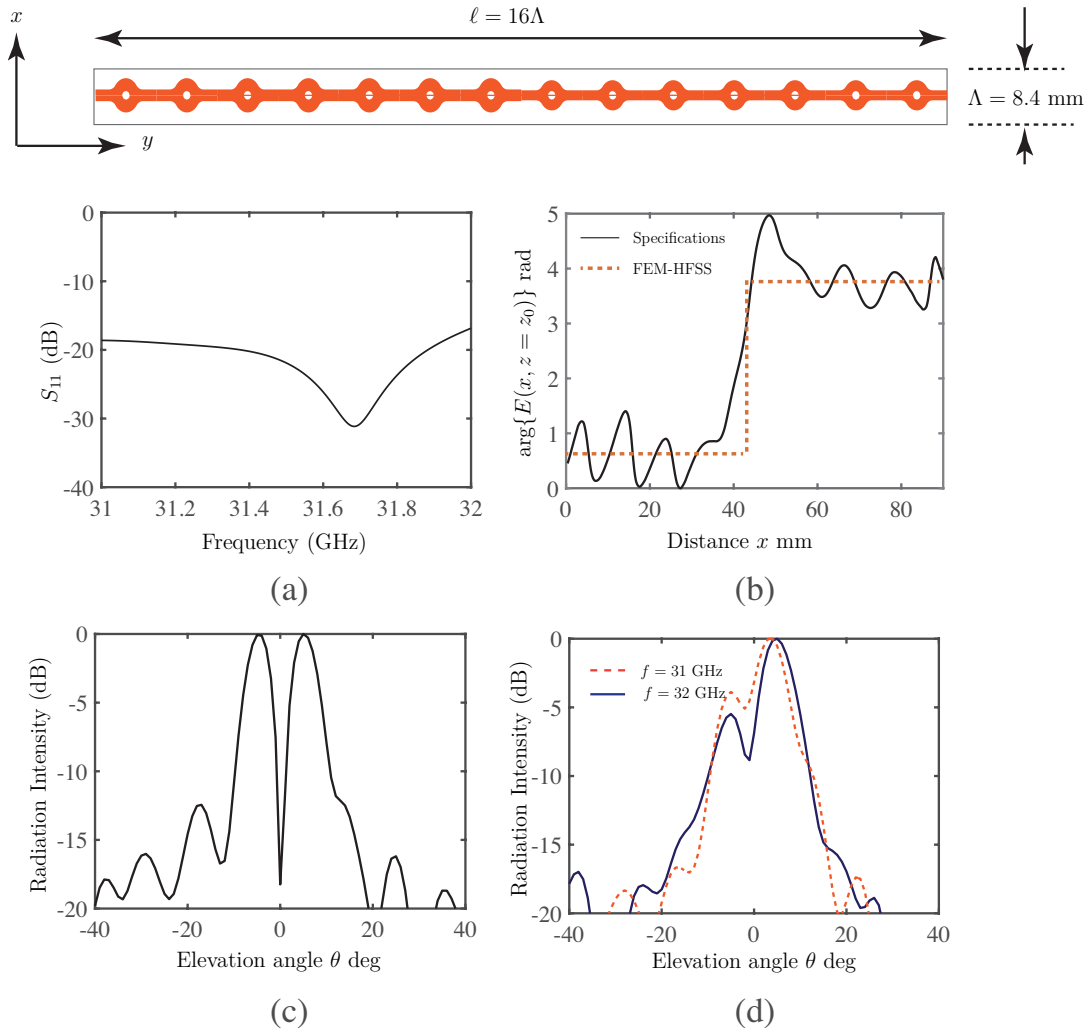


Figure 3.7 FEM-HFSS field results of a Difference-pattern metasurface for beam broadening. a) Reflection response. b) Near-field phase profile at $z_0 = 10$ mm (measured from the metasurface). c) Co-polarized radiation pattern ($E_\phi(\theta)$ at $\phi = 90^\circ$) at the design frequency of 31.5 GHz, and d) at two neighboring frequencies.

to be in good agreement with that predicted by the generalized Snell's law (4.12°). The figure also shows the patterns at neighboring frequencies, where the refraction property is lost and the beams come back to $\theta = 0^\circ$. This is due to the dispersive nature of the dielectric unit cell, where phase variation across space rapidly deviates from the designed linear phase at the design frequency. This indicates that the structure is *functionally* narrowband in nature.

3. Difference Pattern:

In certain applications, it is desired to create a null at broadside ($\theta = 0^\circ$), thereby creating wave illumination in two neighboring zones. Such a beam coverage can be obtained using a difference beam pattern. To achieve a null along broadside, the metasurface array can be divided into two halves, occupied by two groups of unit cells, where each group consists of identical cells. If the transmission phase difference between the two halves is designed to be π radians at the design frequency, the two halves will destructively interfere at the broadside direction. To achieve such coverage, the next example implements a difference-pattern design as shown in Fig. 3.7 with its corresponding response shown below. A π phase jump is observed near the middle of the metasurface structure and a strong null is observed, as expected in the far-field. Again, similar to the generalized refraction example, the difference-pattern is rapidly lost as the input frequency is changed from the design frequency.

4. Lensing Operation:

In various applications such as the GATE system, it is desired to increase the beamwidth of the antenna to increase the coverage region. In this case, the metasurface must be designed as a diverging lens, with a quadratic phase profile (concave) across space. Fig. 3.8 shows the lensing metasurface along with its near and far-field responses. The broadening of the far-field pattern is clearly observed with beam-widths almost twice as compared to that without the metasurface. Figure further shows its response at the neighboring frequencies. While this example shows a diverging beam, a complimentary profile of the quadratic phase can easily be constructed to achieve a focussed beam. The detailed geometrical dimensions of all the three non-uniform metasurfaces are tabulated below.

The above examples of various beam-shaping examples illustrates several important aspects and features of the all-dielectric metasurfaces, and following observations and comments are made and should be noted:

1. No optimizations were performed in designing these metasurfaces. While the unit cell library was constructed using periodic boundary conditions, the unit cell response is

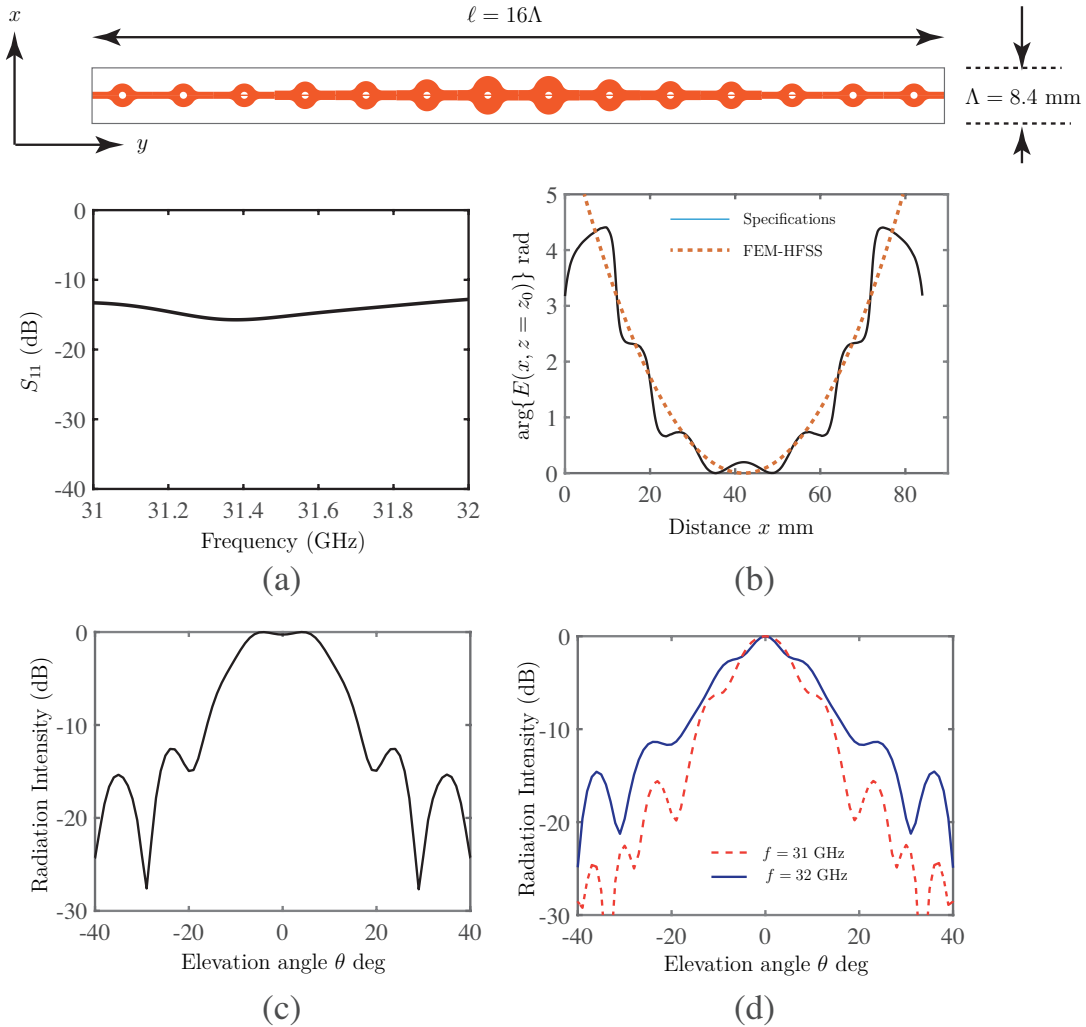


Figure 3.8 FEM-HFSS field results of a Lens metasurface for beam broadening. a) Reflection response. b) Near-field phase profile at $z_0 = 40$ mm. c) Co-polarized radiation pattern ($E_\phi(\theta)$ at $\phi = 90^\circ$) at the design frequency of 31.5 GHz, and d) at two neighboring frequencies.

	τ			R_{out} (mm)			w (mm)		
	GRM	DPM	CONM	GRM	DPM	CONM	GRM	DPM	CONM
Cell #1	1	1.085	1	1.64	1.67	1.64	0.5	0.59	0.5
Cell #2	1.07	1.085	1.12	1.67	1.67	1.7	0.58	0.59	0.66
Cell #3	1.11	1.085	1.13	1.69	1.67	1.73	0.64	0.59	0.68
Cell #4	1.12	1.085	1.16	1.7	1.67	1.91	0.65	0.59	0.71
Cell #5	1.12	1.085	1.2	1.7	1.67	2.23	0.66	0.59	0.73
Cell #6	1.13	1.15	1.2	1.71	1.79	2.23	0.67	0.7	0.73
Cell #7	1.13	1.15	1.16	1.73	1.79	1.91	0.67	0.7	0.71
Cell #8	1.14	1.15	1.13	1.76	1.79	1.73	0.69	0.7	0.68
Cell #9	1.16	1.15	1.12	1.91	1.79	1.7	0.66	0.7	0.66
Cell #10	1.17	1.15	1	1.7	1.79	1.64	0.71	0.7	0.5
	GRM	DPM	CONM	GRM	DPM	CONM	GRM	DPM	CONM

Table 3.1 Ellipticity τ , puck radius R_{out} and bridge thickness w for the three metasurfaces of Fig. 3.6, Fig. 3.7 and Fig. 3.8, corresponding to the generalized refraction metasurface (GRM), Difference Pattern metasurface (DPM) and the concave metasurface (CONM). The unit cell size in all cases is $\Lambda_x = 8.4$ mm.

expected to be perturbed once it is used inside a metasurface where the environment is no more periodic. This is expected to lead to deviations from the ideal phase responses needed in the design. However, a good matching of all the metasurfaces was seen.

2. The all-dielectric metasurface can be designed to exhibit wide variety of wave transformation, with a broadband matching. However, the functional bandwidth defined as the bandwidth where the desired wave transformation is maintained, is found to be small.
3. The lookup table is constructed with only a small set of phase values, and intermediate phase values must be properly interpolated. While this interpolation was not described here, as the focus was to illustrate the metasurface beam forming example, a more detailed procedure will be described in the next chapter.

Chapter 4 Metasurface Demonstration

The previous chapter described the design and wave transformation capabilities of all-dielectric unit cells using an elliptical dielectric resonator. All the designs presented around the 30 GHz frequency band, are within the fabrication capabilities using laser engraved dielectric process used in [2]. While laser engraving is very accurate with very low fabrication tolerances, it is a time consuming and a very costly process. In this thesis, a more traditional approach of engraving the dielectrics is taken in an attempt to realize lower cost all-dielectric metasurfaces, based on *mechanical drilling* or micro-machining of bulk dielectrics. Laser engraving of a 15 cm \times 15 cm sized metasurfaces, was estimated to take about 12 hours¹, as opposed to few hours using mechanical drillings with roughly 20% of the cost. However, the mechanical drilling process is less accurate resulting in a trade-off between time, cost and accuracy. In addition, given the importance of the IEEE 801.11ad frequency band at 60 GHz, we decided to explore the feasibility of such metasurfaces at these frequencies, and estimate the fabrication tolerances. Perfectly aware of the high risk but non-zero potential for success, the implementation of an all-dielectric metasurface around the 60 GHz band was eventually decided. This choice was also motivated due to the fact that an easier access to near-field equipments suitable for metasurface measurements was readily available in the WR-15 band (50 GHz - 75 GHz)².

4.1 All-dielectric Metasurface Design

Our goal now is to design an all-dielectric metasurface which has beam forming and shaping capabilities. Since no standard equipment exist for measuring the scattered fields of a metasurface, it was decided to place the all-dielectric metasurface on top of a 2D slot array antenna similar to the ones of [12], and performing a standard near-field measurements on top of the metasurface, following the beam-forming illustration of Chapter 2. The 2D slot antenna used was a 16 \times 16 array with a unit cell period of $\Lambda_x = 4.2$ mm fabricated using the diffusion bonding process for the 60 GHz band. This fixed the unit cell size of the metasurface to the same value of Λ_x and the metasurface to consist of 16 \times 16 unit cells. Next, the metasurface was decided to be designed for beam-broadening using a quadratic phase profile along one direction of space and uniform along the other direction for simplicity.

¹Using the in-house fabrication facility at Ecole Polytechnique de Montreal, Quebec, Canada.

²All metasurface prototypes and their measurements were conducted in Antenna Research Group of Prof. Hirokawa and Prof. Takashi Tomura, at the Tokyo Institute of Technology, Japan.

The starting point was the construction of the unit cell library to achieve a 2π phase coverage while maintaining good matching. RO 3006 ($\epsilon_r = 6.5$) of thickness 50 mils was used to realize the metasurface. Fig. 4.1(a) shows the simulated transmission phase response of the metasurface unit cell, by varying the unit cell ellipticity, τ , the outside radius R_{out} and the dielectric bridge thickness w . A close to 2π phase coverage is observed around 61 GHz, with good matching below -10 dB in a large bandwidth (not shown here).

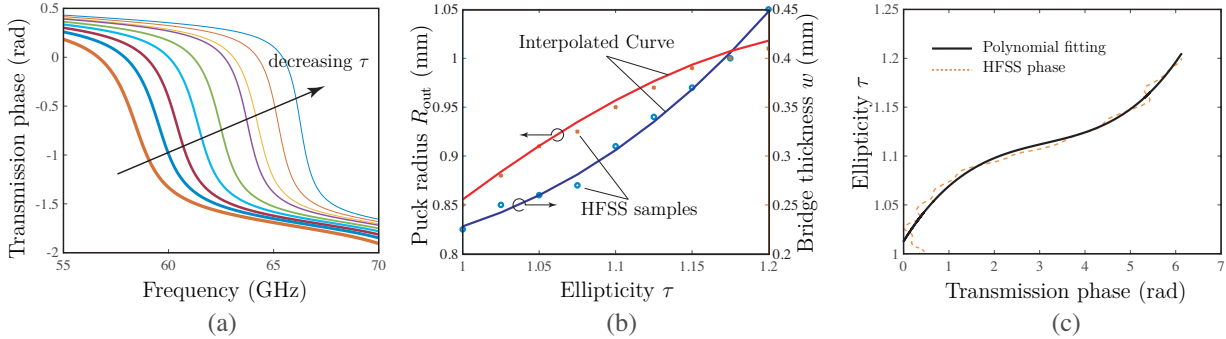


Figure 4.1 The unit cell library used for constructing an all-dielectric metasurface obtained using HFSS. a) Variation of the transmission phase coverage with varying unit cell parameters. b) Relationship between the puck radius and the bridge thickness with the puck ellipticity for several set of matched unit cells. c) Mapping between transmission phase and puck ellipticity at 61 GHz.

Since the intended phase profile of the metasurface is of quadratic shape, 16 different unit cells had to be designed sampling the 2π phase range at the design frequency of 61 GHz. This was achieved as follows. For each ellipticity value τ , the corresponding value of puck radius and bridge thickness, providing a good matching is plotted as shown in Fig. 4.1(b). A one-to-one mapping between τ and the other two parameters is clearly seen. In addition, another plot of transmission phase for every value of ellipticity parameters (9 samples) is constructed as shown in Fig. 4.1(b) for 61 GHz. This data is next curve fitted using a polynomial function to obtain a smooth function as shown in Fig. 4.1(c). Again, a one-to-one mapping between τ and phase is observed. Both plots are obtained using the simulation results of the cells of Fig. 4.1(a). Now, using these two plots, intermediate phase values can be realized by interpolating the physical dimensions of the metasurface. For instance, for any desired phase ϕ_0 , the corresponding ellipticity is determined, which is then used to extract the puck radius and bridge thickness. This will ensure that this combination of physical dimensions lead to matched unit cell exhibiting the desired transmission phase of ϕ_0 . These set of plots thus complete our look-up table for designing the metasurface.

Next, a metasurface model is created with various unit cell dimensions using the look-up table

such that a quadratic phase profile is approximated across it. The FEM-HFSS simulated full-wave responses are shown in Fig. 4.2(a) for the design frequency of 61 GHz along with two neighboring frequencies. A good matching throughout the band was achieved (not shown here). We observe that while an increasing transmission phase is achieved when approaching the edge of the metasurface, the phase deviates significantly from the desired quadratic profile. The corresponding far-field radiation patterns are also shown in Fig. 4.2(b). While a significant broadening of the main beam is observed as was desired, the main beam also exhibits strong nulls, which can be attributed to the poor approximation of the transmission phase.

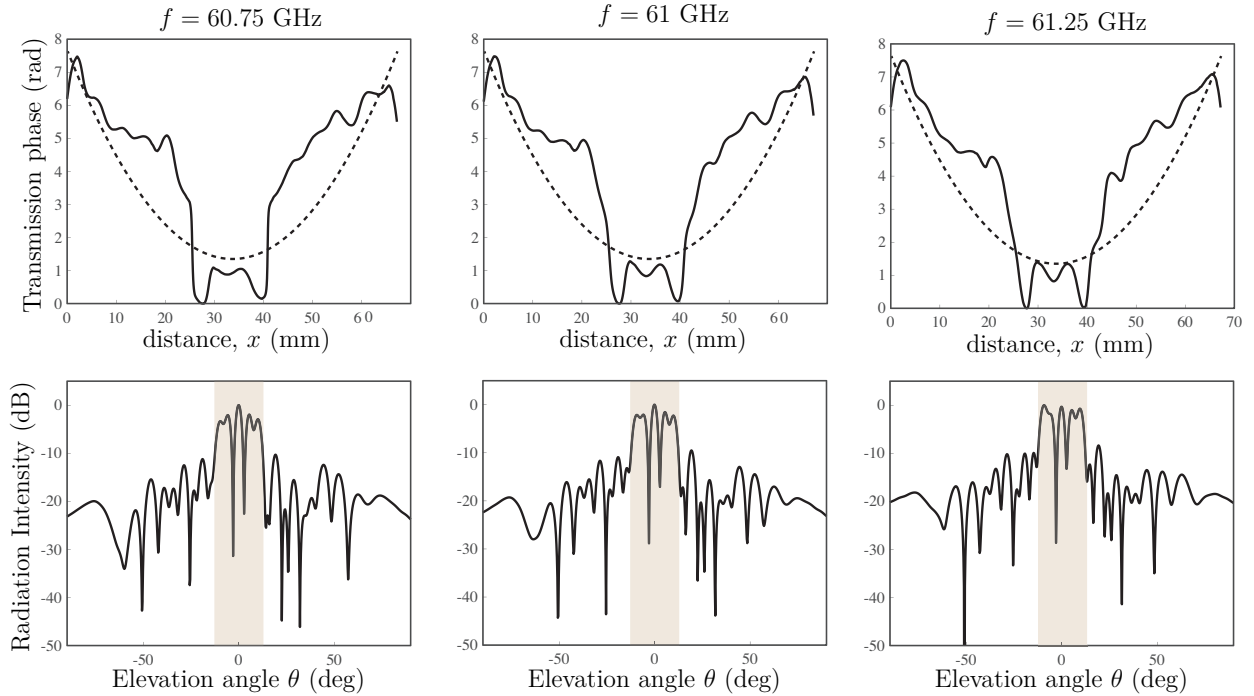


Figure 4.2 Near-field phase distributions and far-field radiation patterns (normalized) of the designed concave lens at the design frequency of 61 GHz along with two neighboring frequencies.

4.2 Experimental Demonstration

To explore the feasibility of the design, it was fabricated using standard mechanical drilling of bulk dielectrics. The picture of the metasurface prototype is shown in Fig. 4.3(a). It consists of 16×16 array of elliptical resonators of varying sizes according to the HFSS profiles of Fig. 4.2. The metasurface is terminated with a dielectric frame around it with mounting screws at the four corners. Next, a 2D planar slot array is used as a source [12]. Metasurface

is then placed on top of the antenna using plastic spacers as shown in Fig. 4.3(b) and the near-fields were measured at few discrete frequencies using a compact near-field measurements system. The spacing between the metasurface and the antenna aperture was set to 2 cm to reduce coupling between metasurface and the antenna. The measured near-fields are then post-processed using the measurement software that computes the standard nearfield-to-farfield transformation to produce the far-field patterns of the antenna.

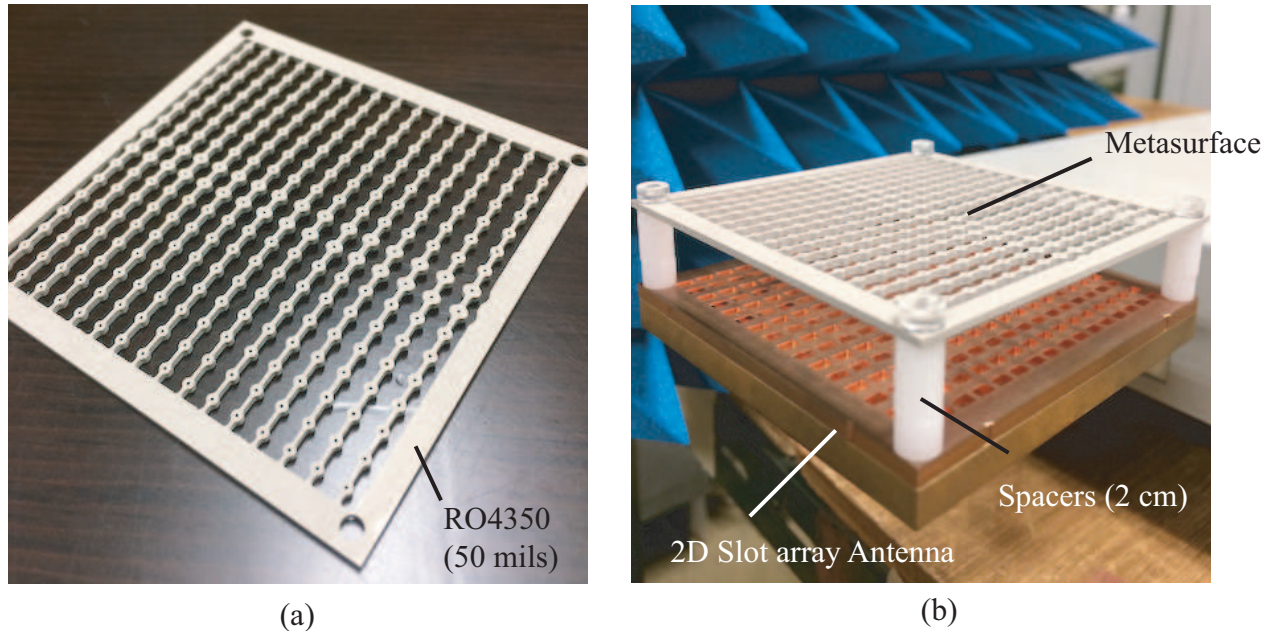


Figure 4.3 All-dielectric metasurface prototype. a) Picture of the fabricated 16×16 metasurface of Fig. 4.2. b) Measurement technique.

For estimating the desired beam-broadening effect of the metasurface, the antenna was measured first without the metasurface. Fig. 4.4 shows the co-polarized far-field patterns at three frequencies, obtained using the near-field measurements showing a main-lobe at $\theta = 0^\circ$ with side-lobe levels typical of uniform aperture antennas. Next, the metasurface is placed on top and the measurements are performed again. A good matching around -10 dB is measured for all three frequencies. The corresponding radiation patterns are superimposed with that of the antenna alone, as shown in Fig. 4.4. A significant broadening of the beam is observed, and several beams are produced near the main lobes. While the usefulness of this pattern is questionable, one of the objectives of performing this exercise was to estimate the feasibility of the design compared to an ideal design. This comparison of the measured versus simulated results (only metasurface using the simulation model of Fig. 3.4) are also shown in Fig. 4.4. The measured results significantly deviate from the simulated ones, while exhibiting similar features. This is a moderate success.

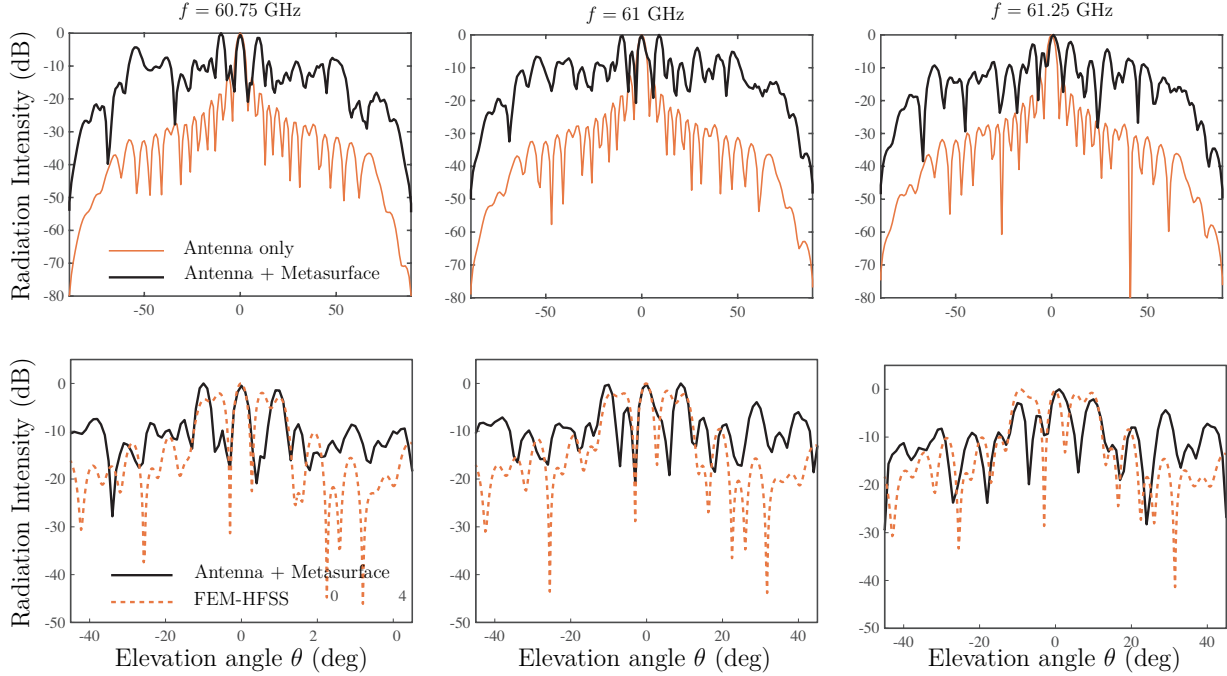


Figure 4.4 Far-field radiation patterns (normalized) obtained from measured near-field response of the metasurface of Fig. 4.3 at three different frequencies, compared with that of slot antenna and FEM-HFSS.

To understand the reason for this discrepancy, the metasurface unit cells were measured under the microscope. Considering the large number of cells (256), and the manual dimensions measurement procedure, key dimensions of few of the unit cells only were measured. A typical measurement picture is shown in Fig. 4.5. Several issues are identified using these measurements. Firstly, several of the unit cells were asymmetric as opposed to ideal elliptical shapes. Secondly, the dielectric wall edges were found to be not smooth exhibiting rough dielectric traces. Thirdly, in several unit cells, the inner hole was offset and not aligned to the elliptical puck. Fourthly, the elliptical cells had rounded edges of approximately 1 mm diameter. Finally, the overall dimensions of the puck had large variations across the metasurface along with variation of the unit cell period ranging from 4.21-4.43 mm (ideally 4.2 mm). For instance, the diameter of the smallest puck at the edge was measured to be $826 \mu\text{m}$ as opposed to $872 \mu\text{m}$ (error of $46 \mu\text{m}$). For the largest puck in the center, it was $1334 \mu\text{m}$ compared to the ideal puck of $1391 \mu\text{m}$ (error of $57 \mu\text{m}$). Both the measurement snapshots are shown in Fig. 4.5. All these factors combined represent several fabrication issues, which may explain the discrepancy between the simulation and measurements results. Moreover, the measurements are done in the presence of the antenna.

To estimate the effect of these fabrication tolerances, the rounding effect (fillet radius of

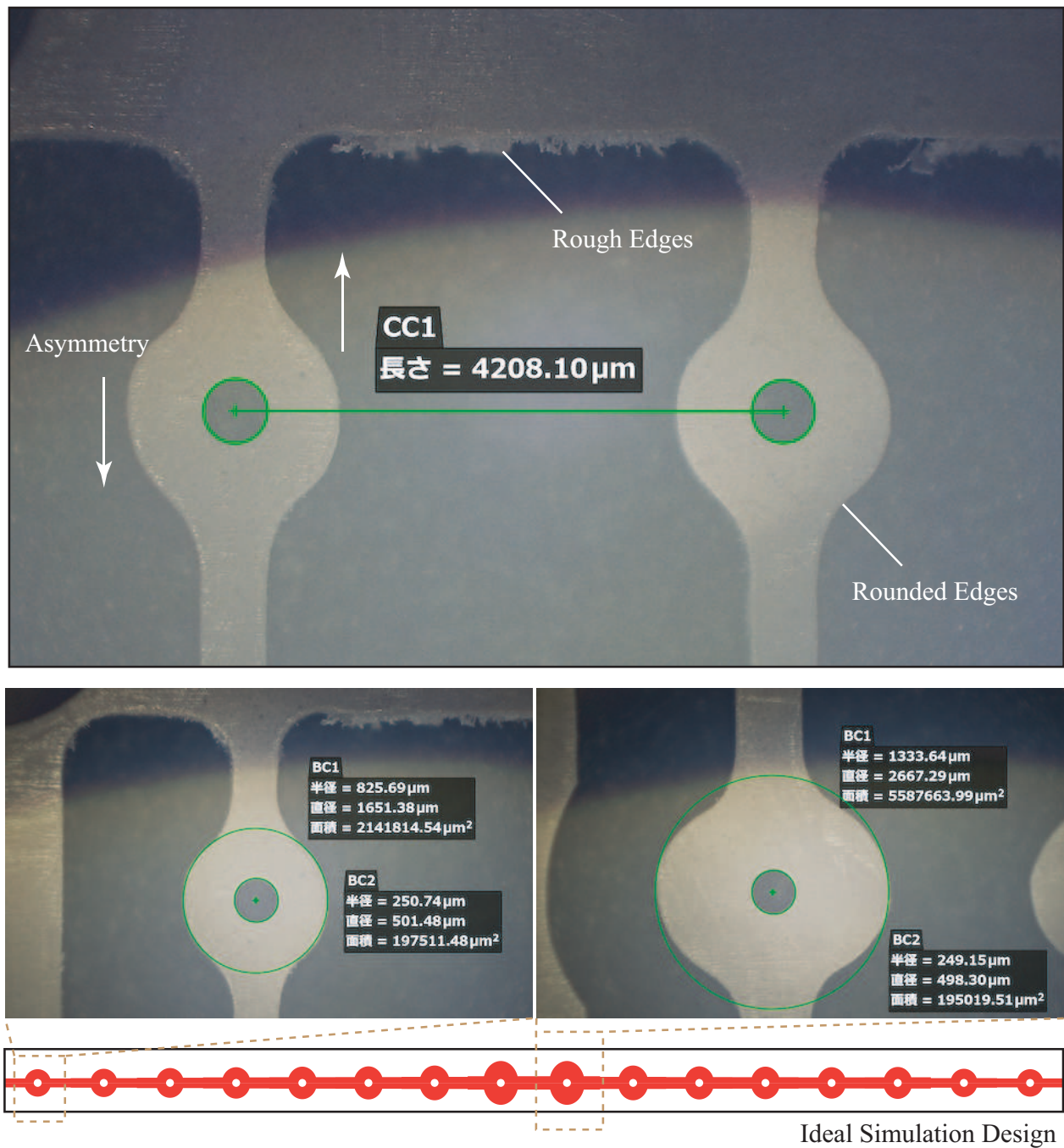


Figure 4.5 Pictures of the metasurface using a microscope to estimate the dimensional tolerances and other fabrication non-idealities.

about 1 mm), period variation (average 0.11 mm) and the over-cutting of the puck radii (average of $50 \mu\text{m}$) were fed back into the HFSS metasurface model. An average of 4.31 mm was used as the unit cell period following the dimensions measurements. Fig. 4.6 shows the recomputed radiation patterns at 61 GHz compared with that of the ideal design and the measured results. It is observed that while the rounding edges and the puck radius has a minor effect, the unit cell period appears to be a critical factor. With an increased average value, a positive trend is observed where the extra main-lobes become higher similar to the ones seen in measurements.

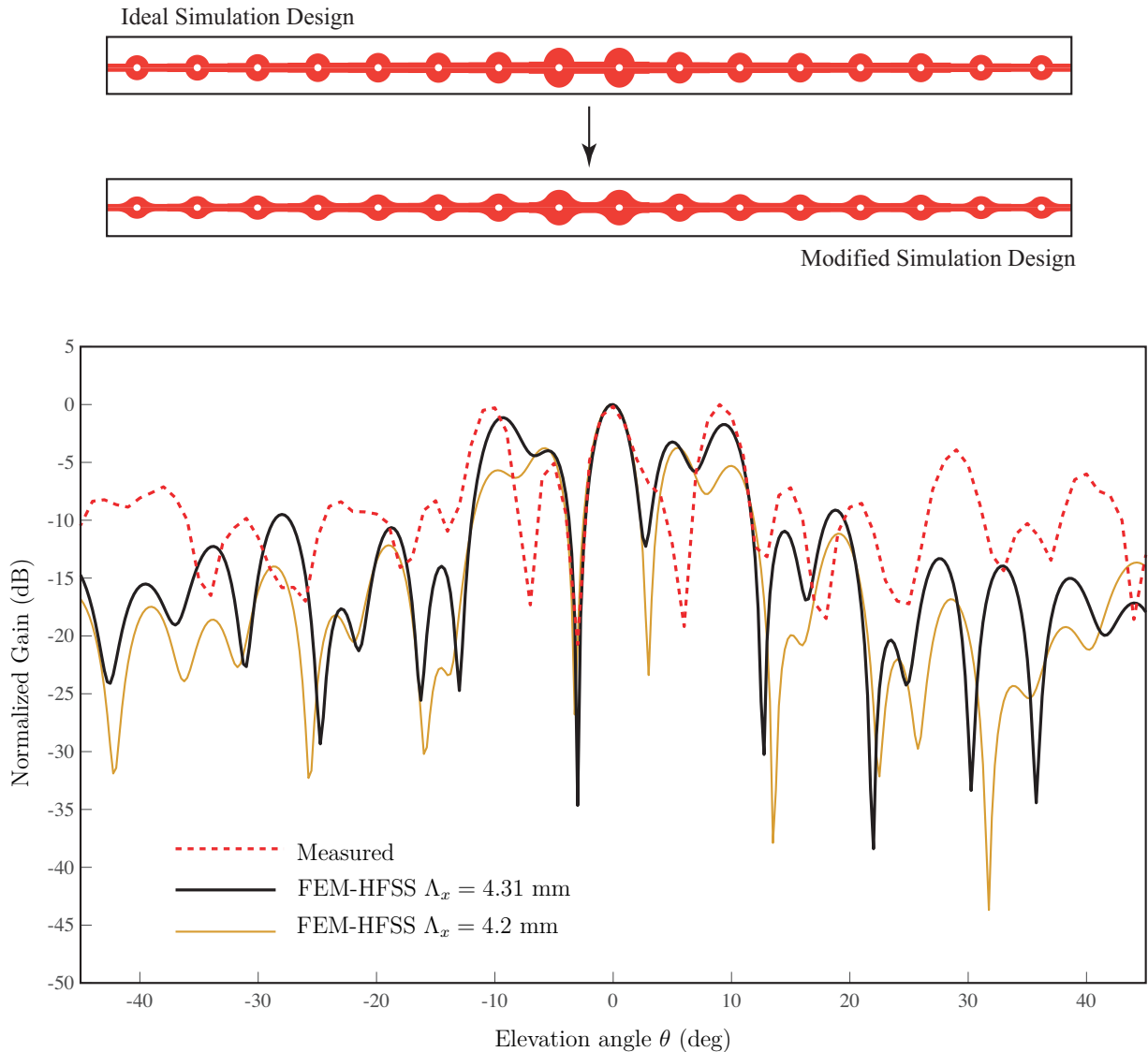


Figure 4.6 Modified HFSS model of the metasurface incorporating the rounded edges, period variation and the over-cutting of the puck.

These fabrication non-idealities are linked to the actual fabrication steps used in manufac-

turing the metasurface. Each row of dielectric resonators connected by the bridges of the metasurface, are fabricated sequentially. As soon as one row was complete, it was held around the centre using a mechanical clip to reduce any mechanical vibrations and distortions of the patterns. However, this was a non-systematic method where holding the dielectric rows become more and more difficult as more rows are machined. Essentially, the bridges are not mechanically strong enough to hold the metasurface in place at these dimensional scales, and withhold the strong mechanical vibrations during the manufacturing process. The large errors in the inner regions (particularly the unit cell period) of the metasurface thus appears to be consistent with this fabrication process.

Chapter 5 Summary & Future Works

5.1 Key Conclusions

This thesis investigated the feasibility of implementing a non-uniform all-dielectric Huygens' metasurfaces at mm-Wave frequencies, which were designed using FEM-HFSS around the 30 and 60 GHz bands, and fabricated around the 60 GHz frequency band using a low-cost micro-machining process for beam-forming applications. This has been the first focussed research effort on Huygens' metasurface using dielectric structures at high frequency bands in the literature, using an elliptical dielectric resonator. This unit cell has been proposed here where the various geometrical dimensions were varied to achieve a 2π phase coverage while maintaining a good matching in a wide frequency range. Compared to the state-of-the-art metasurfaces, all-dielectric Huygens' surfaces are simpler to design due to less number of design variable using a single substrate, thus not requiring a costly multi-layer process. Key conclusions of this work are:

1. The application of Huygens' metasurface for both near- and far-field beam-forming applications is found to be a promising direction of research, particularly in cases, where static beam-forming is desired, the antenna sources are complex to design, are already deployed and costly to manufacture.
2. The all-dielectric implementation of Huygens' metasurface using laser milling (costly and time consuming, but accurate) and micro-machining (low-cost but less accurate) represent non-conventional fabrication processes and represents alternatives for metasurface realizations due to their design simplicity.
3. Wide variety of wave transformations are possible to achieve using all-dielectric metasurfaces as demonstrated by several designs at 30 GHz in Chapter 3.
4. A systematic design procedure has been provided in Chapter 3, to design finite size metasurfaces for specified spatial phase profiles, starting from a unit cell simulation.
5. As an example of mm-wave metasurface, a beam-broadening metasurface around 60 GHz has been fabricated with limited success. Several fabrication issues and large tolerances were observed, which makes the current process and design unsuitable. However, the trends are perceived to be encouraging as the beam-shaping capability was partially observed, just not with the desired accuracy. More investigation is required to resolve these issues and perfect these designs.

5.2 Future Works

While the metasurface demonstration in this thesis is not perfect, but it opens several avenues for future investigation, given there was a gradual increase of some concrete understanding of the issues, and a real potential for real-life applications. Some of the following aspects are worth investigating to refine the art of metasurface designs at mm-waves.

1. In this thesis, no effort was made to optimize the spatial phase distribution in the near-field of the metasurface. The different unit cell responses were obtained using Floquet boundary simulations in a perfectly periodic environment. This was later used to construct the lookup table from which the end result metasurface was formed. This is naturally an approximation as when the metasurface is formed, the unit cells are not in periodic environment anymore. Various unit cells are thus coupled in a more complex way, which leads to distortion in the near-field phase. While this issue is not specific to all-dielectric structures, and is universally true for any metasurface design, it was certainly a factor contributing to a non-ideal phase response (and far-field beam patterns) that are not particularly useful for practical beam-forming applications.
2. The phase engineering of the metasurface should ideally include all nearby couplings along two orthogonal directions of space. This is a computationally challenging requirement. If a routine optimization procedure has to be used to tune the geometrical dimensions of the structure, we need a faster method to compute the scattered fields of the overall metasurface. More research needs to be done for fast and efficient numerical simulation of EM metasurfaces.
3. The Metasurfaces have been used as phase plates in this work, where only the phase distribution in space is engineered. This naturally limits the number of wave transformation possibilities as magnitude is kept uniform across the metasurfaces. A more complete wave transformation also requires an independent modulation of the magnitude in addition to the phase. This may require using different kind of materials such as doped graphene, where there conductivities can be engineered to achieve desired amount of losses in passive designs.
4. The single dielectric design used here operates only on linear-polarized waves. In certain applications, one may require manipulating circular polarizations as well. This may require engineering the cell topology or using cascaded metasurfaces, which may further help in increasing the functional bandwidth of the metasurface.

5. The metasurfaces were designed here as stand-alone devices assuming perfect plane-wave illumination, but were tested when placed in the near-field of the slot array antenna. The metasurface was thus illuminated with a finite-sizes quasi-uniform plane wave. For more accurate design, the metasurface unit cells must be simulated in the presence of the slot array, and taking into account the edge effects due to the finite size of the antenna aperture. The edge effects can be reduced to a certain extent by making the metasurface larger than the radiating aperture, which however comes at an expense of costlier fabrication.
6. The biggest challenge in this work was the fabrication procedure used. The fabrication errors in realizing various dimensions, such as puck size, rounded corners, unit cell period etc, prompts a more in-depth characterization of the fabrication process. An alternative approach is to modify the metasurface design to make it more mechanically stable by using two orthogonal bridges as opposed to one used in this work. In that case, the EM effect of bridges must be carefully evaluated. In addition, the PCB based Huygens' metasurfaces must also be designed and tested at these frequencies exhibiting similar phase and transmission characteristics, for a fair comparison with the all-dielectric structures in terms of tolerances, cost and loss performances.

In summary, this research has explored an alternative design and fabrication of all-dielectric metasurfaces at mm-wave frequencies, as compared to the conventional PCB based process, and envisioned their application for antenna beam-forming by manipulating the near-fields of the antenna. More research work is needed to compare the electrical performance of all-dielectric Huygens' surfaces compared to the PCB ones. Although the presented research here introduces more questions than providing answers, the results are encouraging, and opens exciting directions in mm-wave research related to exotic wave propagation phenomenon.

Bibliography

- [1] M. Decker, I. Staude, M. Falkner, J. Dominguez, D. N. Neshev, I. Brener, T. Pertsch, and Y. S. Kivshar, “High-efficiency dielectric Huygens’ surfaces,” *Adv Opt Mater.*, vol. 3, no. 6, pp. 813–820, 2015.
- [2] K. Achouri, A. Yahyaoui, S. Gupta, H. Rmili, and C. Caloz, “Dielectric resonator metasurface for dispersion engineering,” *IEEE Trans. Antennas Propag.*, vol. 65, no. 2, pp. 673–680, 2017.
- [3] X. Wan, S. L. Jia, T. J. Cui, and Y. J. Zhao, “Independent modulations of the transmission amplitudes and phases by using Huygens’ metasurfaces,” *Scient. Rep.*, vol. 6, 2016.
- [4] C. Pfeiffer and A. Grbic, “Metamaterial Huygens’ surfaces: Tailoring wave fronts with reflectionless sheets,” *Phys. Rev. Lett.*, vol. 110, p. 197401, May 2013.
- [5] Huawei, “5G: A technology vision,” *White Paper*, 2013.
- [6] F. Boccardi, R. W. Heath, A. Lozano, T. L. Marzetta, and P. Popovski, “Five disruptive technology directions for 5G,” *IEEE Comm. Mag.*, vol. 52, no. 2, pp. 74–80, February 2014.
- [7] T. S. Rappaport, S. Sun, R. Mayzus, H. Zhao, Y. Azar, K. Wang, G. N. Wong, J. K. Schulz, M. Samimi, and F. Gutierrez, “Millimeter wave mobile communications for 5G cellular: It will work!” *IEEE Access*, vol. 1, pp. 335–349, 2013.
- [8] I. Richard H. Roy and B. Ottersten, “Spatial division multiple access wireless communication systems,” *US Patent US5515378 A*, 1991.
- [9] A. Lozano and N. Jindal, “Transmit diversity vs. spatial multiplexing in modern mimo systems,” *Trans. Wireless. Comm.*, vol. 9, no. 1, pp. 186–197, Jan. 2010.
- [10] C. Holloway, E. F. Kuester, J. Gordon, J. O’Hara, J. Booth, and D. Smith, “An overview of the theory and applications of metasurfaces: The two-dimensional equivalents of MTMs,” *IEEE Antennas Propag. Mag.*, vol. 54, no. 2, pp. 10–35, April 2012.
- [11] M. Zhang, K. Toyosaki, J. Hirokawa, M. Ando, T. Taniguchi, and M. Noda, “A 60-GHz band compact-range gigabit wireless access system using large array antennas,” *IEEE Trans. Antennas Propag.*, vol. 63, no. 8, pp. 3432–3440, Aug 2015.

- [12] T. Tomura, J. Hirokawa, T. Hirano, and M. Ando, "A 45°linearly polarized hollow-waveguide 16 × 16-slot array antenna covering 71-86 GHz band," *IEEE Trans. Antennas Propagat.*, vol. 62, no. 10, pp. 5061–5067, Oct 2014.
- [13] T. Tomura, Y. Miura, M. Zhang, J. Hirokawa, and M. Ando, "A 45°linearly polarized hollow-waveguide corporate-feed slot array antenna in the 60-GHz band," *IEEE Trans. Antennas Propagat.*, vol. 60, no. 8, pp. 3640–3646, Aug 2012.
- [14] J. Hirokawa, T. Tomura, M. Zhang, and M. Ando, "Plate-laminated waveguide slot array antennas for wideband and high-gain operations," in *2014 XXXIth URSI General Assembly and Scientific Symposium (URSI GASS)*, Aug 2014, pp. 1–1.
- [15] M. Sano, J. Hirokawa, and M. Ando, "A hollow rectangular coaxial line for slot array applications fabricated by diffusion bonding of laminated thin metal plates," *IEEE Trans. Antennas Propag.*, vol. 61, no. 4, pp. 1810–1815, April 2013.
- [16] C. L. Holloway, A. Dienstfrey, E. F. Kuester, J. F. O'Hara, A. K. Azad, and A. J. Taylor, "A discussion on the interpretation and characterization of metafilms/metasurfaces: The two-dimensional equivalent of metamaterials," *Metamaterials*, vol. 3, no. 2, pp. 100–112, 2009.
- [17] S. Jahani and Z. Jacob, "All-dielectric metamaterials," *Nat. Nanotechnol.*, vol. 11, p. 23–36, 01 2016.
- [18] F. Capolino, *Theory and phenomena of metamaterials*. CRC press, 2009.
- [19] N. Yu, P. Genevet, M. A. Kats, F. Aieta, J.-P. Tetienne, F. Capasso, and Z. Gaburro, "Light propagation with phase discontinuities: generalized laws of reflection and refraction," *Science*, p. 1210713, 2011.
- [20] N. Fang, H. Lee, C. Sun, and X. Zhang, "Sub-diffraction-limited optical imaging with a silver superlens," *Science*, vol. 308, no. 5721, pp. 534–537, 2005.
- [21] Z. Liu, H. Lee, Y. Xiong, C. Sun, and X. Zhang, "Far-field optical hyperlens magnifying sub-diffraction-limited objects," *Science*, vol. 315, no. 5819, pp. 1686–1686, 2007.
- [22] R. A. Shelby, D. R. Smith, and S. Schultz, "Experimental verification of a negative index of refraction," *Science*, vol. 292, no. 5514, pp. 77–79, 2001.
- [23] V. M. Shalaev, W. Cai, U. K. Chettiar, H.-K. Yuan, A. K. Sarychev, V. P. Drachev, and A. V. Kildishev, "Negative index of refraction in optical metamaterials," *Opt. Lett.*, vol. 30, no. 24, pp. 3356–3358, 2005.

- [24] D. Schurig, J. Mock, B. Justice, S. A. Cummer, J. B. Pendry, A. Starr, and D. Smith, “Metamaterial electromagnetic cloak at microwave frequencies,” *Science*, vol. 314, no. 5801, pp. 977–980, 2006.
- [25] J. Valentine, J. Li, T. Zentgraf, G. Bartal, and X. Zhang, “An optical cloak made of dielectrics,” *Nat. Mat.*, vol. 8, no. 7, p. 568, 2009.
- [26] T. Ergin, N. Stenger, P. Brenner, J. B. Pendry, and M. Wegener, “Three-dimensional invisibility cloak at optical wavelengths,” *Science*, p. 1186351, 2010.
- [27] A. Sihvola, “Metamaterials in electromagnetics,” *Metamaterials*, vol. 1, no. 1, pp. 2–11, 2007.
- [28] R. Grimberg, “Electromagnetic metamaterials,” *Materials Science and Engineering: B*, vol. 178, no. 19, pp. 1285–1295, 2013.
- [29] E. Shamonina and L. Solymar, “Metamaterials: How the subject started,” *Metamaterials*, vol. 1, no. 1, pp. 12–18, 2007.
- [30] H.-T. Chen, A. J. Taylor, and N. Yu, “A review of metasurfaces: physics and applications,” *Reports on Progress in Physics*, vol. 79, no. 7, p. 076401, 2016.
- [31] C. L. Holloway, E. F. Kuester, J. A. Gordon, J. O’Hara, J. Booth, and D. R. Smith, “An overview of the theory and applications of metasurfaces: The two-dimensional equivalents of metamaterials,” *IEEE Antennas Propag. Mag.*, vol. 54, no. 2, pp. 10–35, April 2012.
- [32] S. B. Glybovski, S. A. Tretyakov, P. A. Belov, Y. S. Kivshar, and C. R. Simovski, “Metasurfaces: From microwaves to visible,” *Phys. Rep.*, vol. 634, pp. 1–72, 2016.
- [33] C. Pfeiffer and A. Grbic, “Bianisotropic metasurfaces for optimal polarization control: Analysis and synthesis,” *Phys. Rev. Appl.*, vol. 2, no. 4, p. 044011, 2014.
- [34] E. Hasman, V. Kleiner, G. Biener, and A. Niv, “Polarization dependent focusing lens by use of quantized pancharatnam–berry phase diffractive optics,” *Appl. Phys. Lett.*, vol. 82, no. 3, pp. 328–330, 2003.
- [35] Z. Bomzon, G. Biener, V. Kleiner, and E. Hasman, “Space-variant pancharatnam–berry phase optical elements with computer-generated subwavelength gratings,” *Opt. Lett.*, vol. 27, no. 13, pp. 1141–1143, 2002.

- [36] E. Hasman, Z. Bomzon, A. Niv, G. Biener, and V. Kleiner, “Polarization beam-splitters and optical switches based on space-variant computer-generated subwavelength quasi-periodic structures,” *Opt. Com.*, vol. 209, no. 1-3, pp. 45–54, 2002.
- [37] Y.-H. Lee, G. Tan, T. Zhan, Y. Weng, G. Liu, F. Gou, F. Peng, N. V. Tabiryan, S. Gauza, and S.-T. Wu, “Recent progress in pancharatnam–berry phase optical elements and the applications for virtual/augmented realities,” *Optical Data Processing and Storage*, vol. 3, no. 1, pp. 79–88, 2017.
- [38] S. Choudhury, U. Guler, A. Shaltout, V. M. Shalaev, A. V. Kildishev, and A. Boltasseva, “Pancharatnam–berry phase manipulating metasurface for visible color hologram based on low loss silver thin film,” *Adv Opt Mater.*, vol. 5, no. 10, p. 1700196, 2017.
- [39] X. Ni, N. K. Emani, A. V. Kildishev, A. Boltasseva, and V. M. Shalaev, “Broadband light bending with plasmonic nanoantennas,” *Science*, vol. 335, no. 6067, pp. 427–427, 2012.
- [40] N. M. Estakhri and A. Alù, “Wave-front transformation with gradient metasurfaces,” *Phys. Rev. X*, vol. 6, no. 4, p. 041008, 2016.
- [41] J. Cheng, D. Ansari-Oghol-Beig, and H. Mosallaei, “Wave manipulation with designer dielectric metasurfaces,” *Opt. Lett.*, vol. 39, no. 21, pp. 6285–6288, 2014.
- [42] X. Ni, A. V. Kildishev, and V. M. Shalaev, “Metasurface holograms for visible light,” *Nat. Com.*, vol. 4, p. 2807, 2013.
- [43] N. Yu, F. Aieta, P. Genevet, M. A. Kats, Z. Gaburro, and F. Capasso, “A broadband, background-free quarter-wave plate based on plasmonic metasurfaces,” *Nano Lett.*, vol. 12, no. 12, pp. 6328–6333, 2012.
- [44] H. Mosallaei and K. Sarabandi, “A one-layer ultra-thin meta-surface absorber,” in *Antennas and Propagation Society International Symposium, 2005 IEEE*, vol. 1. IEEE, 2005, pp. 615–618.
- [45] R. Alaee, M. Albooyeh, M. Yazdi, N. Komjani, C. Simovski, F. Lederer, and C. Rockstuhl, “Magnetolectric coupling in nonidentical plasmonic nanoparticles: Theory and applications,” *Phys. Rev. B*, vol. 91, no. 11, p. 115119, 2015.
- [46] C. Pfeiffer, C. Zhang, V. Ray, L. J. Guo, and A. Grbic, “Polarization rotation with ultra-thin bianisotropic metasurfaces,” *Optica*, vol. 3, no. 4, pp. 427–432, 2016.

- [47] N. Yu and F. Capasso, “Flat optics with designer metasurfaces,” *Nat. Mat.*, vol. 13, no. 2, p. 139, 2014.
- [48] T. S. Almong and O. M. Ramahi, “Metamaterial electromagnetic energy harvester with near unity efficiency,” *Appl. Phys. Lett.*, vol. 106, no. 15, p. 153902, 2015.
- [49] J. A. Gordon, C. L. Holloway, J. Booth, S. Kim, Y. Wang, J. Baker-Jarvis, and D. R. Novotny, “Fluid interactions with metafilms/metasurfaces for tuning, sensing, and microwave-assisted chemical processes,” *Phys. Rev. B*, vol. 83, no. 20, p. 205130, 2011.
- [50] M. Farmahini-Farahani and H. Mosallaei, “Birefringent reflectarray metasurface for beam engineering in infrared,” *Opt. Lett.*, vol. 38, no. 4, pp. 462–464, 2013.
- [51] T. Niu, W. Withayachumnankul, A. Upadhyay, P. Gutruf, D. Abbott, M. Bhaskaran, S. Sriram, and C. Fumeaux, “Terahertz reflectarray as a polarizing beam splitter,” *Opt. Ex.*, vol. 22, no. 13, pp. 16 148–16 160, 2014.
- [52] K. Achouri and C. Caloz, “Recent developments in metasurface design and applications,” in *2017 XXXII Ind General Assembly and Scientific Symposium of the International Union of Radio Science (URSI GASS)*. IEEE, 2017, pp. 1–4.
- [53] B. Liu, K. Song, and J. Xiao, “Two-dimensional optical metasurfaces: From plasmons to dielectrics,” *Advances in Condensed Matter Physics*, vol. 2019, 2019.
- [54] F. Ding, Y. Yang, R. A. Deshpande, and S. I. Bozhevolnyi, “A review of gap-surface plasmon metasurfaces: fundamentals and applications,” *Nanophotonics*, vol. 7, no. 6, pp. 1129–1156, 2018.
- [55] M. I. Shalaev, J. Sun, A. Tsukernik, A. Pandey, K. Nikolskiy, and N. M. Litchinitser, “High-efficiency all-dielectric metasurfaces for ultracompact beam manipulation in transmission mode,” *Nano Lett.*, vol. 15, no. 9, pp. 6261–6266, 2015.
- [56] A. V. Kildishev, A. Boltasseva, and V. M. Shalaev, “Planar photonics with metasurfaces,” *Science*, vol. 339, no. 6125, p. 1232009, 2013.
- [57] J. Li, S. Chen, H. Yang, J. Li, P. Yu, H. Cheng, C. Gu, H.-T. Chen, and J. Tian, “Simultaneous control of light polarization and phase distributions using plasmonic metasurfaces,” *Adv. Funct. Mat.*, vol. 25, no. 5, pp. 704–710, 2015.

- [58] K. Achouri, B. A. Khan, S. Gupta, G. Lavigne, M. A. Salem, and C. Caloz, “Synthesis of electromagnetic metasurfaces: principles and illustrations,” *arXiv preprint arXiv:1510.05997*, 2015.
- [59] A. Ahmadi and H. Mosallaei, “Physical configuration and performance modeling of all-dielectric metamaterials,” *Phys. Rev. B*, vol. 77, no. 4, p. 045104, 2008.
- [60] Y. Yang, I. I. Kravchenko, D. P. Briggs, and J. Valentine, “All-dielectric metasurface analogue of electromagnetically induced transparency,” *Nat. Comm.*, vol. 5, p. 5753, 2014.
- [61] Y. F. Yu, A. Y. Zhu, R. Paniagua-Domínguez, Y. H. Fu, B. Luk’yanchuk, and A. I. Kuznetsov, “High-transmission dielectric metasurface with 2π phase control at visible wavelengths,” *Laser & Photonics Reviews*, vol. 9, no. 4, pp. 412–418, 2015.
- [62] D. Lin, P. Fan, E. Hasman, and M. L. Brongersma, “Dielectric gradient metasurface optical elements,” *Science*, vol. 345, no. 6194, pp. 298–302, 2014.
- [63] S. V. Hum and J. Perruisseau-Carrier, “Reconfigurable reflectarrays and array lenses for dynamic antenna beam control: A review,” *IEEE Trans. Antennas Propag.*, vol. 62, no. 1, pp. 183–198, 2014.
- [64] J. Huang, “Capabilities of printed reflectarray antennas,” in *Proceedings of International Symposium on Phased Array Systems and Technology*. IEEE, 1996, pp. 131–134.
- [65] C. G. Ryan, M. R. Chaharmir, J. Shaker, J. R. Bray, Y. M. Antar, and A. Ittipiboon, “A wideband transmitarray using dual-resonant double square rings,” *IEEE Trans. Antennas Propag.*, vol. 58, no. 5, pp. 1486–1493, 2010.
- [66] D. Berry, R. Malech, and W. Kennedy, “The reflectarray antenna,” *IEEE Trans. Antennas Propag.*, vol. 11, no. 6, pp. 645–651, 1963.
- [67] B. A. Munk, *Frequency selective surfaces: theory and design*. John Wiley & Sons, 2005.
- [68] A. Arbabi, Y. Horie, A. J. Ball, M. Bagheri, and A. Faraon, “Subwavelength-thick lenses with high numerical apertures and large efficiency based on high-contrast transmitarrays,” *Nat. Comm.*, vol. 6, p. 7069, 2015.
- [69] P. R. West, J. L. Stewart, A. V. Kildishev, V. M. Shalaev, V. V. Shkunov, F. Strohkendl, Y. A. Zakharenkov, R. K. Dodds, and R. Byren, “All-dielectric subwavelength metasurface focusing lens,” *Opt. Ex.*, vol. 22, no. 21, pp. 26 212–26 221, 2014.

- [70] A. Arbabi, Y. Horie, M. Bagheri, and A. Faraon, “Dielectric metasurfaces for complete control of phase and polarization with subwavelength spatial resolution and high transmission,” *Nat. Nanotechnol.*, vol. 10, no. 11, p. 937, 2015.
- [71] H. Yang, X. Cao, F. Yang, J. Gao, S. Xu, M. Li, X. Chen, Y. Zhao, Y. Zheng, and S. Li, “A programmable metasurface with dynamic polarization, scattering and focusing control,” *Sc. Rep.*, vol. 6, p. 35692, 2016.
- [72] A. M. Niknejad, “Siliconization of 60 Ghz,” *IEEE Microw. Mag.*, vol. 11, no. 1, pp. 78–85, 2010.
- [73] C. Pfeiffer and A. Grbic, “Millimeter-wave transmitarrays for wavefront and polarization control,” *IEEE Trans. Microw. Theory Tech.*, vol. 61, no. 12, pp. 4407–4417, 2013.
- [74] I. Yoon and J. Oh, “Millimeter wave thin metasurface enabling polarization-controlled beam shaping,” in *Antennas and Propagation & USNC/URSI National Radio Science Meeting, 2017 IEEE International Symposium on.* IEEE, 2017, pp. 669–670.
- [75] J. Oh, “Millimeter-wave short-focus thin lens employing disparate filter arrays,” *IEEE Antennas and Wireless Propagation Letters*, vol. 15, pp. 1446–1449, 2016.
- [76] —, “Millimeter-wave thin lens employing mixed-order elliptic filter arrays,” *IEEE Trans. Antennas Propag.*, vol. 64, no. 7, pp. 3222–3227, 2016.
- [77] Y.-X. Sun and K. W. Leung, “Millimeter-wave substrate-based dielectric reflectarray,” *IEEE Antennas and Wireless Propagation Letters*, vol. 17, no. 12, pp. 2329–2333, 2018.
- [78] T. J. Cui, R. Y. Wu, W. Wu, C. B. Shi, and Y. B. Li, “Large-scale transmission-type multifunctional anisotropic coding metasurfaces in millimeter-wave frequencies,” *Journal of Physics D: Applied Physics*, vol. 50, no. 40, p. 404002, 2017.
- [79] J. Oettler, V. S. Schmid, N. Zankl, O. Rey, A. Dress, and J. Heinze, “Fermat’s principle of least time predicts refraction of ant trails at substrate borders,” *PloS one*, vol. 8, no. 3, p. e59739, 2013.
- [80] Z. Wang, Y. Sun, L. Han, and D. Liu, “General laws of reflection and refraction for subwavelength phase grating,” *arXiv preprint arXiv:1312.3855*, 2013.
- [81] L. Huang, X. Chen, H. Mühlenbernd, H. Zhang, S. Chen, B. Bai, Q. Tan, G. Jin, K.-W. Cheah, C.-W. Qiu, *et al.*, “Three-dimensional optical holography using a plasmonic metasurface,” *Nat. Comm.*, vol. 4, p. 2808, 2013.

- [82] X. Ni, S. Ishii, A. V. Kildishev, and V. M. Shalaev, “Ultra-thin, planar, babinet-inverted plasmonic metalenses,” *Light: Science & Applications*, vol. 2, no. 4, p. e72, 2013.
- [83] X. Chen, L. Huang, H. Mühlenbernd, G. Li, B. Bai, Q. Tan, G. Jin, C.-W. Qiu, S. Zhang, and T. Zentgraf, “Dual-polarity plasmonic metalens for visible light,” *Nat. Comm.*, vol. 3, p. 1198, 2012.
- [84] S. Larouche, Y.-J. Tsai, T. Tyler, N. M. Jokerst, and D. R. Smith, “Infrared metamaterial phase holograms,” *Nat. Mat.*, vol. 11, no. 5, p. 450, 2012.
- [85] Y.-W. Huang, W. T. Chen, W.-Y. Tsai, P. C. Wu, C.-M. Wang, G. Sun, and D. P. Tsai, “Aluminum plasmonic multicolor meta-hologram,” *Nano letters*, vol. 15, no. 5, pp. 3122–3127, 2015.
- [86] G. Zheng, H. Mühlenbernd, M. Kenney, G. Li, T. Zentgraf, and S. Zhang, “Metasurface holograms reaching 80% efficiency,” *Nat. Nanotechnol.*, vol. 10, no. 4, p. 308, 2015.
- [87] S. A. Kuznetsov, M. A. Astafev, M. Beruete, and M. Navarro-Cía, “Planar holographic metasurfaces for terahertz focusing,” *Sci. Rep.*, vol. 5, p. 7738, 2015.
- [88] X. Ni, A. V. Kildishev, and V. M. Shalaev, “Metasurface holograms for visible light,” *Nat. Comm.*, vol. 4, p. 2807, 2013.
- [89] C. R. de Galarreta, A. Alexeev, J. Bertolotti, and C. D. Wright, “Phase-change metasurfaces for dynamic beam steering and beam shaping in the infrared,” in *2018 IEEE International Symposium on Circuits and Systems (ISCAS)*. IEEE, 2018, pp. 1–5.
- [90] M. Selvanayagam and G. V. Eleftheriades, “Discontinuous electromagnetic fields using orthogonal electric and magnetic currents for wavefront manipulation,” *Opt. Ex.*, vol. 21, no. 12, pp. 14 409–14 429, 2013.
- [91] C. Pfeiffer and A. Grbic, “Metamaterial Huygens’ surfaces: Tailoring wave fronts with reflectionless sheets,” *Phys. Rev. Lett.*, vol. 110, p. 197401, May 2013.
- [92] M. Chen, M. Kim, A. M. Wong, and G. V. Eleftheriades, “Huygens’ metasurfaces from microwaves to optics: a review,” *Nanophotonics*, vol. 7, no. 6, pp. 1207–1231, 2018.
- [93] J. P. Wong, M. Selvanayagam, and G. V. Eleftheriades, “Design of unit cells and demonstration of methods for synthesizing Huygens’ metasurfaces,” *Photonics and Nanostructures-Fundamentals and Applications*, vol. 12, no. 4, pp. 360–375, 2014.

- [94] F. S. Cuesta, I. A. Faniayeu, V. S. Asadchy, and S. A. Tretyakov, "Planar broadband Huygens' metasurfaces for wave manipulations," *IEEE Trans. Antennas Propag.*, vol. 66, no. 12, pp. 7117–7127, 2018.
- [95] A. Arbabi, Y. Horie, M. Bagheri, and A. Faraon, "Complete control of polarization and phase of light with high efficiency and sub-wavelength spatial resolution," *arXiv preprint arXiv:1411.1494*, pp. 4308–4315, 2014.
- [96] A. J. Ollanik, J. A. Smith, M. J. Belue, and M. D. Escarra, "High-efficiency all-dielectric Huygens' metasurfaces from the ultraviolet to the infrared," *ACS Photonics*, vol. 5, no. 4, pp. 1351–1358, 2018.
- [97] L. Zou, W. Withayachumnankul, C. M. Shah, A. Mitchell, M. Bhaskaran, S. Sriram, and C. Fumeaux, "Dielectric resonator nanoantennas at visible frequencies," *Opt. Ex.*, vol. 21, no. 1, pp. 1344–1352, 2013.
- [98] A. Howes, W. Wang, I. Kravchenko, and J. Valentine, "Dynamic transmission control based on all-dielectric Huygens' metasurfaces," *Optica*, vol. 5, no. 7, pp. 787–792, 2018.
- [99] A. Forouzmand, M. M. Salary, S. Inampudi, and H. Mosallaei, "A tunable multigate indium-tin-oxide-assisted all-dielectric metasurface," *Adv Opt Mater.*, vol. 6, no. 7, p. 1701275, 2018.
- [100] A. Epstein and G. V. Eleftheriades, "Arbitrary power-conserving field transformations with passive lossless omega-type bianisotropic metasurfaces," *IEEE Trans. Antennas Propag.*, vol. 64, no. 9, pp. 3880–3895, 2016.
- [101] K. Achouri, M. A. Salem, and C. Caloz, "General metasurface synthesis based on susceptibility tensors," *IEEE Trans. Antennas Propag.*, vol. 63, no. 7, pp. 2977–2991, 2015.
- [102] D. M. Pozar, "Microwave engineering 3e," *Transmission Lines and Waveguides*, pp. 143–149, 2005.